Background information on vdsim, the

Vortex Dynamics SIMulation

Hans Fangohr, November 2002

Header: /Users/svn/cvs/VD/V1Docu/V1docu/userguide/main.tex,v 1.1.1.1 2002/11/05 18:14:10 fangohr Exp

Abstract

An overview of the Vortex Dynamics SIMulation package is given.

- Chapter 1 gives some background on the vortex state (just a summary from other works).
- Chapter 2 shows some equations being used in the simulation, and demonstrates some of the internals of the simulation.
- In chapter 3 we show that the long-range nature of the vortex-vortex interaction can result in numerical artefacts, and provide two techniques to overcome these problems: (i) using a 'smooth' cut-off which reduces the interaction force near the cut-off smoothly to zero, and (ii) an infinite lattice summation technique applicable for a K_0-Bessel function interaction potential.

  This is mainly the content of *Fangohr et al.* (2000) with some more details. In addition, we describe the nearest neighbour look-up and the pre-computation of the interaction table for infinite lattice summations as can be used in the simulation software.
- More details and simulation results obtained using the simulation can be found in:
  - *Fangohr, de Groot and Cox* (2001b) Vortex dynamics in two-dimensional systems at high driving forces. *Physical Review B*, **64**, 064505 (2001a).
  - *Fangohr, Cox and de Groot* (2001a) Critical transverse forces in weakly pinned driven vortex systems. *Physical Review B*, **63**, 064501 (2001b).
  - *Fangohr, Koshelev and Dodgson* (2002) Vortex matter in layered superconductors without josephson coupling: numerical simulations within mean field approach. *cond-mat/0210580* (2002). Submitted to Phys. Rev. B.

Contents

List of Tables

List of Figures

Chapter 1

The vortex state

1.1 Superconductivity

Kamerlingh Onnes found in 1911 that the electrical resistance of Mercury drops below any measurable value when it was cooled below a critical temperature of $T_c = 4.2$ K. This effect was christened "superconductivity" and many more elements and compounds have been found to become superconducting at sufficiently low temperatures, including the recently discovered magnesium diboride (*Nagamatsu et al.*, 2001). The critical temperature T_c below which the superconductivity exists has been increased up to well above 100 K in the late 1980s after the discovery by *Bednorz and Müller* (1986) of a new class of cuprate superconductors.

The understanding of conventional type-I superconductors, which expel an external magnetic field completely, is relatively good. In 1935 *London and London* proposed equations which govern the behaviour of microscopic electric and magnetic fields and introduced the characteristic length λ, which is now called the London penetration depth. *Bardeen, Cooper and Schrieffer* (BCS) produced their Nobel prize winning theory of superconductivity in 1957 from which the London equations can be derived. It states that there is a phonon-mediated attraction between superconducting electrons. Two electrons with equal but opposite momentum and spin can form a so-called "Cooper pair". The spatial extension of such a pair is given by the *Pippard* coherence length (1953), and the Cooper pairs are separated from the normal conducting electrons by an energy gap.

Already in 1950 *Ginzburg and Landau* published their theory which is based on Landau's general theory of phase transitions. They introduced a complex pseudo-wave-function ψ as an order parameter which measures the "superconducting order" and derived differential equations which couple ψ and the magnetic vector potential. Ginzburg and Landau introduced the Ginzburg-Landau coherence length $\xi(T)$ which, sufficiently far below T_c, is similar to the temperature independent Pippard coherence length. It has been shown subsequently that the Ginzburg-Landau theory is a limiting form of a suitably generalised BCS-theory (*Gorkov*, 1959). The ratio of the London penetration depth, λ, and the Ginzburg-Landau coherence length, ξ, defines the Ginzburg-Landau parameter $\kappa = \lambda/\xi$.

The quantitative description of the high-temperature superconductors is based on the phenomenological Ginzburg-Landau theory, Abrikosov's work on the vortex state (as described in section 1.2), and Gorkov's work. It is therefore occasionally referenced as the GLAG-description. However, a theoretical description of the pairing mechanism giving rise to superconductivity is still lacking.

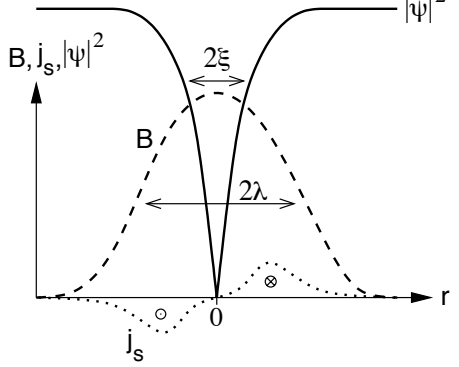

Figure 1.1: Spatial variation of the Cooper pair density $|\psi|^2$, the magnetic induction B, and the supercurrent j_s around the vortex centre. The magnetic induction drops to zero over the length scale given by the London penetration depth, λ, and the superconducting order parameter, ψ, varies on the length scale ξ.

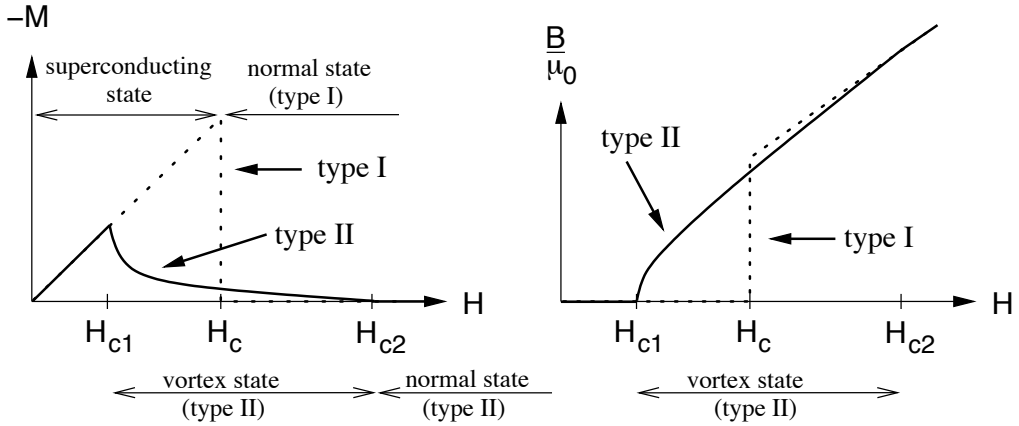

Figure 1.2: Different behaviour of magnetisation M *(left)* and magnetic induction B *(right)* to an external applied magnetic field H in type-I and type-II superconductors. In type-II superconductors, vortices start penetrating the material at H_{c1} and represent B within the sample. At H_{c2} the vortex cores overlap and the external field H_{c2} is established as superconductivity breaks down.

1.2 The vortex state

In 1957 *Abrikosov* investigated theoretically what would happen if the Ginzburg-Landau parameter, κ, was larger than 1, in contrast to being much smaller than 1, as it is for classical pure superconductors. He found that the surface energy of an interface of a superconducting and a normal region would be negative. It turned out that a sample of such a material being exposed to a magnetic field (near the upper critical field H_{c2}) would be subdivided into smaller and smaller domains of alternating superconducting and non-superconducting regions to reduce the system's overall energy. Abrikosov called these materials "type-II" superconductors because their behaviour differs strongly from the classical type-I superconductors.

It is now established that the normal regions are tube-like flux lines which penetrate a type-II superconductor in the form of a regular triangular array (in the absence of any disordering effects). Each of these flux lines, which are also called vortices, carries a magnetic flux quantum $\Phi_0 = h/2e$, with h being Planck's constant and e the electron charge. Each flux line is surrounded by a supercurrent screening the enclosed magnetic induction. Figure 1.1 shows the magnetic induction and the superconducting order parameter in the neighbourhood of a vortex.

Type-I superconductors with $\kappa < 1/\sqrt{2}$ expel an external magnetic field completely up to a critical field value H_c at which the superconductivity breaks down, as demonstrated schematically in figure 1.2 (dotted line). Type-II superconductors show the same behaviour for small

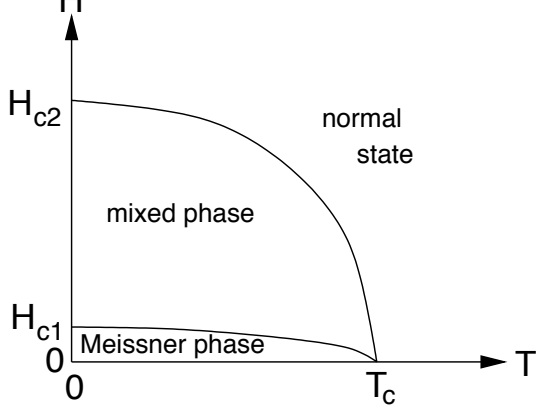

Figure 1.3: Phase diagram of type-II superconductor

fields but only up to field strengths $H_{c1} < H_c$. For field strengths between H_{c1} and H_{c2}, the external field penetrates the bulk in the form of vortices. This regime is called the "vortex state" or the "mixed state" and it is this situation which has been investigated in this work. Because of the partial flux penetration, the diamagnetic energy cost of expelling the field is reduced and therefore H_{c2} can be significantly larger than H_c. This property has made high-field superconductors possible.

In the mixed state, vortices tend to align in a hexagonal lattice to minimise their energy.

The critical fields $H_{\rm c1}$ and $H_{\rm c2}$ are functions of the temperature and decrease with increasing temperature. In figure 1.3 we show the phase diagram of a type-II superconductor as a function of magnetic field and temperature. At zero temperature, we can estimate $H_{\rm c1} \approx \frac{1}{\kappa} H_{\rm c}$ and $H_{\rm c2} \approx \kappa H_{\rm c}$ (*Kittel*, 1996). For high-temperature-materials, the Ginzburg-Landau parameter is big ($\kappa_{\rm YBCO} \approx 90$ and $\kappa_{\rm BSCCO} \approx 60$) and therefore $H_{\rm c1}$ is much smaller than shown in figure 1.2 and 1.3.

In this work the regime $H \gg H_{c1}$ is investigated and hence $B \approx \mu_0 H$, where μ_0 is the free-space permeability. For convenience both the magnetic field H and the magnetic induction B are referred to as magnetic fields.

1.3 Interactions in the vortex state

1.3.1 Lorentz force and flux flow

In the presence of a transport current, a Lorentz force $\mathbf{f}_{\rm L}$ per unit length, proportional to the current density $\mathbf{j}$ acts on the vortices and pushes them in a direction perpendicular to the transport current and perpendicular to the orientation of the magnetic field

$$\mathbf{f}_{\rm L} = \mathbf{j} \times \mathbf{\Phi}_0, \tag{1.1}$$

where $\mathbf{\Phi}_0$ is a vector pointing in the direction of the magnetic field with a magnitude of the magnetic flux quantum Φ_0.

For an ideal homogeneous material, *Bardeen and Stephen* (1965) showed that the resulting motion of vortices with velocity v is resisted by a viscous drag force $f_{\rm visc} = -\eta_{\rm volume} v$ per unit volume with a viscosity coefficient $\eta_{\rm volume}$ per unit volume given by

$$\eta_{\rm volume} = B^2/\rho_{\rm ff} \qquad \text{and} \qquad \rho_{\rm ff} \approx \rho_n B/B_{c2}, \tag{1.2}$$

with $\rho_{\rm ff}$ the flux flow resistivity, ρ_n the normal state resistivity of the material, B the magnetic induction, and B_{c2} the upper critical value of B at which superconductivity breaks down. Equation (1.2) has been confirmed in experiments, for example by *Kunchur et al.* (1993). The normal

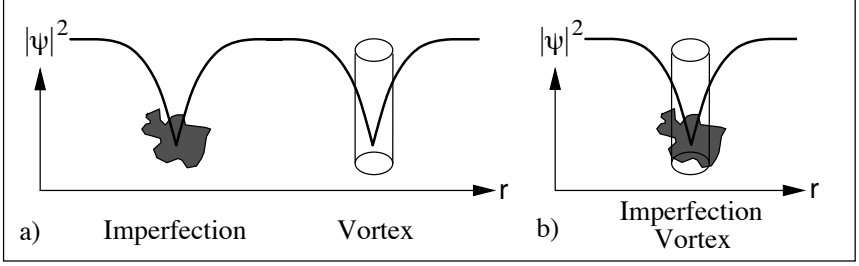

Figure 1.4: a) Schematic plot of the density of Cooper pairs in the neighbourhood of an imperfection in the crystal structure and a vortex. b) If the vortex is placed into the imperfection then the system's energy is reduced.

state resistivity enters the expression because the moving vortices induce local electric fields (due to the magnetic induction changing with time) which act on the unpaired non-superconducting electrons. There is another contribution coming from the change of the Cooper pair density on a time scale comparable to the relaxation time of the Cooper pair system (*Buckel*, 1993, p.181).

If vortices move, they dissipate energy which is taken from the transport current. This manifests itself as a voltage across the material, and in such circumstances the material has a resistance.

1.3.2 Pinning

In practice, real materials always have inhomogeneities, which tend to "pin" vortices to the atomic crystal structure. Therefore, for currents below a critical current density, the vortices are pinned and do not respond to a small Lorentz force, so no resistance is measured.

Imperfections in the crystal structure influence the motion of vortices via scattering or the suppression of the superconducting order parameter (*Blatter et al.*, 1994, p.1143). The latter mechanism can be explained qualitatively in terms of the energy contribution of the condensation energy to the superconducting state and is illustrated in figure 1.4. Imperfections in the periodicity of the atomic structure locally inhibit superconductivity. In these areas, there is no negative contribution from the condensation energy to the total energy of the superconducting state. The net reduction in system energy of a vortex in a type-II superconductor is positive, and the core of the vortex is not superconducting. It is therefore energetically advantageous if a vortex is located in an imperfection. Any attempt to move it from there to another position would increase the system energy. For forces which are not too large the vortex is pinned.

There are different kinds of pinning objects in high-temperature superconductors such as $YBa_2Cu_3O_{7-\delta}$ (YBCO). On the atomic scale, there are oxygen vacancies which locally suppress the superconducting order parameter and appear spatially uncorrelated. On the other hand, there are correlated defects such as twin boundaries due to the orthorhombic structure of YBCO which separate domains in which the crystal a- and b-directions interchange roles. These twin planes and other extended defects such as grain boundaries, stacking faults, screw dislocations, and sample surfaces are larger pinning objects and can pin more than one vortex strongly. Finally, using ionising radiation, columnar defects can be created which can also be relatively strong pinning centres if a vortex aligns with the defect.

1.3.3 Vortex-vortex interactions

In addition to the Lorentz force and the pinning interaction a third force acting on vortices is their mutual repulsion.

All high-temperature superconductors known to date, such as YBCO and $Bi_2Sr_2CaCu_2O_8$ (BSCCO), are layered materials, *i.e.* superconducting CuO_2 layers alternate with less superconducting layers. A vortex line can be understood as a coupled line of two-dimensional "pancake" vortices which occupy the CuO_2 layers (*Artemenko and Kruglov*, 1990, *Feigel'man et al.*, 1990, *Buzdin and Feinberg*, 1990, *Clem*, 1991). The following is a short summary of the different kinds of electromagnetic interaction between pancake vortices in single and stacked two-dimensional layers (*Clem*, 1991, *Blatter et al.*, 1994, pp.1277, *Clem*, 1998).

1.3.3.1 Two pancake vortices in an isolated superconducting thin film

The energy $U(r)$ of two pancake vortices separated by a distance $r = \sqrt{x^2 + y^2}$ in a thin film of thickness d is given by Pearl's solution (*Pearl*, 1964)

$$U(r) = \frac{\Phi_0^2 d}{2\pi\mu_0\lambda_s^2}\left(H_0\left(\frac{r}{\Lambda}\right) - Y_0\left(\frac{r}{\Lambda}\right)\right) \tag{1.3}$$

where $\lambda_s \approx 1000\text{Å}$ is the London bulk penetration depth, and $\Lambda = 2\lambda_s^2/d \approx 3 \cdot 10^5\text{Å}$ is the two-dimensional thin film screening length. The quoted numbers are characteristic of an YBCO layer and are given to provide a feel for the order of magnitude of the different lengths. H_0 and Y_0 are the Struve function and the Bessel function of the second kind.

The bulk penetration depth, λ_s relates to the in-plane penetration depth of a thin layer, $\lambda_{ab} \approx 1400\text{Å}$, via $\lambda_s = \lambda_{ab}\sqrt{d/s}$, where $d \approx 6\text{Å}$ is the layer thickness and $s \approx 12\text{Å}$ is the layer spacing. We re-write $\Lambda = 2\lambda_{ab}^2/s$, and introduce

$$\epsilon_0 = \frac{\Phi_0^2}{4\pi\mu_0\lambda_{ab}^2}, \tag{1.4}$$

with $\mu_0 = 4\pi \cdot 10^{-7}\frac{\text{Vs}}{\text{Am}}$ being the vacuum permeability and Φ_0 the magnetic flux quantum. Eventually, we can express the interaction (1.3) strength in terms of ϵ_0

$$U(r) = 2\epsilon_0 s\left(H_0\left(\frac{r}{\Lambda}\right) - Y_0\left(\frac{r}{\Lambda}\right)\right). \tag{1.5}$$

For small and large r, the following approximations hold:

$$U(r) \propto -\ln\left(\tfrac{r}{\Lambda}\right) \quad : \quad r \ll \Lambda \tag{1.6}$$

$$U(r) \propto \tfrac{1}{r} \quad : \quad r \gg \Lambda. \tag{1.7}$$

1.3.3.2 Two pancake vortices in one layer in a system of stacked thin films

Due to induced screening currents in the layers above and below the "central" layer (which holds one pancake vortex), the resulting current distributions are different from those in the isolated thin film. For the repulsive force between two vortices in one layer in an infinite system of stacked layers it has been shown (*Clem*, 1991, eqn. 27) that the interaction force $F(r)$ is given by

$$F(r) = 2\epsilon_0 s\frac{1}{r}\left[1 - \frac{\lambda_{ab}}{\Lambda}\left(1 - \exp\left(-\frac{r}{\lambda_{ab}}\right)\right)\right]. \tag{1.8}$$

Since $\lambda_{ab}/\Lambda \approx 10^{-3}$, this is effectively

$$F_r(r) = \frac{2\epsilon_0 s}{r}. \tag{1.9}$$

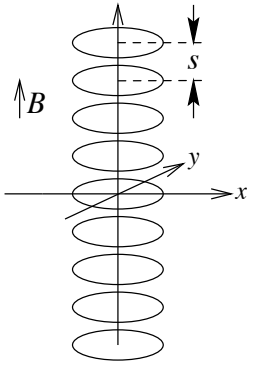

Figure 1.5: A stack of aligned two-dimensional vortex pancakes.

This corresponds to a potential

$$U(r) = -2\epsilon_0 s \ln(r) \tag{1.10}$$

which is logarithmic at all distances, not just for $r \ll \Lambda$ as in the isolated thin film (1.6).

For the electromagnetic interaction of two pancake vortices in different layers an attractive force is found that is weaker than the in-layer repulsion by a factor of approximately $\lambda_{\mathrm{ab}}/\Lambda$. We consider this in detail for the studies of three-dimensional pancake systems in *Fangohr et al.* (2002).

1.3.3.3 Two stacks of aligned pancake vortices

For aligned stacks of pancake vortices where the magnetic field is perpendicular to the superconducting planes as shown in figure 1.5, the interaction energy per unit length between two such stacks is found to be

$$U(r) = 2\epsilon_0 K_0\left(\frac{r}{\lambda_{\mathrm{ab}}}\right). \tag{1.11}$$

K_0 is the modified Bessel function of the second kind. Equation (1.11) shows the same r-dependence as the result derived from the London theory for the interaction energy of two vortex lines in a continuous medium (*Tinkham*, 1996, p. 154). In the latter result λ_{ab} is given by λ_s, the isotropic London penetration depth. $K_0(r/\lambda_{\mathrm{ab}})$ can be approximated with

$$K_0\left(\frac{r}{\lambda_{\mathrm{ab}}}\right) = \begin{cases} \sqrt{\frac{\pi\lambda}{2r}}\exp\left(-\frac{r}{\lambda_{\mathrm{ab}}}\right) & : \quad r \to \infty \\ \ln\left(\frac{\lambda_{\mathrm{ab}}}{r}\right) + 0.12 & : \quad r \ll \lambda. \end{cases} \tag{1.12}$$

In contrast to equation (1.10) the interaction energy drops off exponentially for large distances. This is due to the weak attraction of pancakes in different layers.

In the remainder of this work, we are dealing with λ_{ab} rather than λ_s. We therefore use $\lambda \equiv \lambda_{\mathrm{ab}}$ to shorten our notation.

The other interaction which is important for vortex pancakes is the Josephson coupling of pancake vortices between different layers. This contribution has to be considered for a complete treatment of layered superconductors (*Clem*, 1991). A theoretical model is given by *Lawrence and Doniach* (1971) which is a discrete version of the Ginzburg-Landau theory. This has been further investigated by *Bulaevskii et al.* (1992) who found that three- and four-body interactions between pancakes have to be considered. However, the electromagnetic interactions alone provide highly complex physics. Restricting the model to eletromagnetic interactions is justified in the quasi-two dimensional case of rigid vortices in thin-films and for individual layers of pancakes, and it is a fair first approximation for simulations of three-dimensional loosely coupled materials such as BSCCO *Fangohr et al.* (2002).

1.3.4 Summary

The vortex state is determined by the relative strengths of the following energies:

- the vortex-vortex interaction which favours a hexagonal lattice,
- the vortex-pinning energy which (generally) introduces disorder and
- the thermal energy which destabilises the lattice further.

The Lorentz force drives the system over the pinning energy surface and this results in complex vortex dynamics.

Chapter 2

The Simulation

This chapter describes some parts of the computer simulation. The central idea is to represent vortices as massless classical particles that are free to move in a two-dimensional area. Those particles can be identified with vortex-lines when modelling thin films in which vortices are "stiff". To model three-dimensional systems we associate these particles with pancake-vortices, and use a mean field approach (*Fangohr et al.*, 2002) account for interactions in the third dimension.

In section 2.1, an overview of techniques to simulate many-body problems is given and in section 2.2 these techniques are related to the vortex state, followed by a detailed description of the simulation software. This includes the derivation of the central equations of motion in section 2.3 and methods to solve them (section 2.5). In sections 2.6 we describe the boundary conditions and section 2.7 details our choice of simulation units. Section 2.8 assesses the applicability of the model, and in section 2.9 the observables to monitor the simulation are introduced. Section 2.10 concentrates on practical aspects of the usage of the simulation software such as the user interface, and hardware and software requirements. A summary is provided in section 2.11.

2.1 Computer simulations of many-body systems

Computer simulations have proved to be a valuable tool for problems that cannot be solved analytically. Numerical solutions are particularly useful for providing results for specific parameters which are not at all obtainable otherwise.

Following *Haile* (1997), the simulations used to study many-particle problems can be ordered from stochastic simulations to deterministic models as shown in figure 2.1 on the next page.

Monte Carlo simulations are adopted from general Monte Carlo methods for solving high-dimensional integrals. In Monte Carlo simulations the integrals of interest are the statistical mechanics ensemble averages for a property $f(\mathbf{r}^N)$, for example in the canonical ensemble:

$$< f >= \frac{\int \ldots \int \mathrm{d}\mathbf{r_1}\,\mathrm{d}\mathbf{r_2}\ldots\mathrm{d}\mathbf{r_N}\;\; f\left(\mathbf{r}^N\right)\,\exp\left(-\frac{U(\mathbf{r}^N)}{k_\mathrm{B}T}\right)}{\int \ldots \int \mathrm{d}\mathbf{r_1}\,\mathrm{d}\mathbf{r_2}\ldots\mathrm{d}\mathbf{r_N}\;\; \exp\left(-\frac{U(\mathbf{r}^N)}{k_\mathrm{B}T}\right)}. \tag{2.1}$$

This is the standard case where the number of particles N, the temperature T, and the volume V of the simulation are given. The vector $\mathbf{r}^N$ has Nd components when each particle's position $\mathbf{r}_i$ has d components, and $U(\mathbf{r}^N)$ is the energy of the system. Since Monte Carlo methods are generally not well suited to study dynamical quantities, the integration in phase space over the generalised momenta $\mathbf{p}_1, \ldots, \mathbf{p}_N$ has been carried out already in equation (2.1).

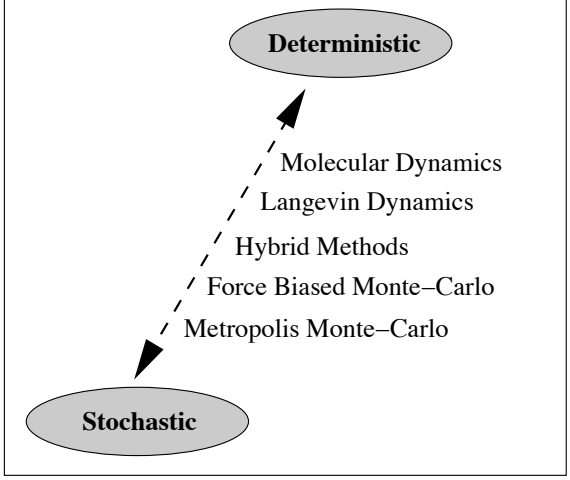

Figure 2.1: Monte Carlo simulations work stochastically and molecular dynamics simulations work deterministically. There are various techniques that combine both methods.

Taking the Boltzmann factor $\exp\left(-\frac{U(\mathbf{r}^N)}{k_\mathrm{B}T}\right)$ into account, it was suggested by *Metropolis et al.* (1953) to consider only configurations which contribute most to the integral. This is known as importance sampling for general Monte Carlo methods and in the context of Monte Carlo simulations it is referred to as the "Metropolis algorithm".

Particle positions are altered by trial moves which are conditionally accepted. Each new configuration depends only on the previous one and is achieved by moving one particle a small distance to a new position which is determined by a random number generator. The configurations encountered in the run of a simulation are obtained stochastically.

Molecular dynamics methods can be divided into equilibrium and non-equilibrium dynamics. Equilibrium dynamics are usually applied in the micro-canonical ensemble to an isolated system with energy E, containing a fixed number of particles N, in a fixed volume V. However, there exist methods to fix the simulated temperature, which allows investigation of canonical ensembles (for example *Rapaport*, 1995). In non-equilibrium molecular dynamics, an external force is applied to the system to establish non-equilibrium situations of interest. The particles' positions are obtained by integrating Newton's equation of motion. For a set of N particles with positions $\mathbf{r}_i$, the set of equations to solve reads[1]

$$m_i\ddot{\mathbf{r}}_i = \mathbf{F}_i\left(\mathbf{r}_{1,\ldots,N}, \dot{\mathbf{r}}_{1,\ldots,N}, t\right) \qquad \mathrm{i} = 1, \ldots, \mathrm{N}, \tag{2.2}$$

where m_i is the mass of particle i, and $\mathbf{F}_i$ is the total force acting on i. The velocity of particle i is $\dot{\mathbf{r}}_i$ and $\ddot{\mathbf{r}}_i$ is its acceleration.

To compute a system property $f(\mathbf{r}^N, \dot{\mathbf{r}}^N)$, one takes the time average of that property

$$< f >= \lim_{t\to\infty} \frac{1}{t} \int_{t_0}^{t_0+t} \mathrm{d}t' \; f\left(\mathbf{r}^N(t'), \dot{\mathbf{r}}^N(t')\right). \tag{2.3}$$

In contrast to the Monte Carlo simulations, it is here easily possible to investigate dynamical quantities such as transport coefficients and time correlation functions. According to the ergodicity hypothesis the ensemble average in equation (2.1) and the time average in equation (2.3) should be the same.

Force biased Monte Carlo methods compute the force exerted from all other particles on particle i and then move that particle i in this direction. This reduces the number of trial moves required, but each sweep is computationally more expensive.

[1]The following convention is used: the dot notation represents the time derivative: $\dot{\mathbf{r}} = \frac{\mathrm{d}\mathbf{r}}{\mathrm{d}t}$ and $\ddot{\mathbf{r}} = \frac{\mathrm{d}^2\mathbf{r}}{\mathrm{d}t^2}$.

Hybrid methods are Monte Carlo simulations that use a sequence of molecular dynamics steps to generate new random configurations. This ensures that very different areas in phase space are covered and reduces the number of Monte Carlo sweeps required to study equilibrium properties of the system.

Langevin dynamics were developed to investigate Brownian Motion (*Lenk and Gellert*, 1989, p.537). One studies particles immersed in a continuum, for example a fluid. Instead of considering all microscopic interactions of all particles establishing the fluid, one concentrates on one particle and its interactions with the continuum. The force exerted on the particle by the fluid is broken into two parts: an average viscous force $-\eta\dot{\mathbf{r}}_i$ and a random force $\boldsymbol{\chi}(t)$ whose time average is zero (*Kubo et al.*, 1985, p.14). The equation of motion for particle i is

$$m_i\ddot{\mathbf{r}}_i = -\eta\dot{\mathbf{r}}_i + \boldsymbol{\chi}_i + \mathbf{F}'_i, \tag{2.4}$$

where $\mathbf{F}'_i$ represents all forces not covered in the other two terms. The macroscopic frictional force represents an averaged value of many microscopic interactions. In cases where inertial effects are small, the mass m_i of the particles can be set to zero. That reduces the system of differential equations of second order in (2.4) to a system of first order equations which are occasionally referred to as the "overdamped" Langevin equations of motion because the absence of the inertial term causes the motion to be overdamped.

2.2 Methods to simulate the vortex state

The most direct method to investigate the vortex state is to solve the (time-dependent) Ginzburg-Landau differential equations numerically to obtain solutions for the complex valued order parameter ψ and the magnetic vector potential. The set of coupled non-linear partial differential equations can be solved on a discrete grid, as demonstrated for example by *Braun et al.* (1996), *Gropp et al.* (1996) and *Aranson and Vinokur* (1998). On the one hand this approach does not simplify the physical situation, but on the other hand it is computationally very demanding since it requires many grid points to resolve even a single vortex.

Another starting point is to treat vortices as structureless point- or string-like objects. Each of the areas in which the superconducting order parameter ψ drops to zero is mapped to such an object, which is then considered as being a classical particle. To compute the interactions between these classical particles one uses effective interaction potentials (for example *Clem*, 1991, *Bulaevskii et al.*, 1992). The price which has to be paid for decreasing the computational complexity is that the small length scale ξ is lost and phenomena like pinning, vortex-anti-vortex creation or flux cutting do not come intrinsically with these models, but have to be implemented by other means. To study the statics of the vortex state, Monte Carlo simulations can be used (for example *Täuber and Nelson*, 1995, *Yates et al.*, 1995, *Ryu and Stroud*, 1996), whereas to study the dynamics, Langevin dynamics methods are required (for example *Brass et al.*, 1989, *Koshelev and Vinokur*, 1994, *Grønbech-Jensen et al.*, 1996, *Groth et al.*, 1996, *Moon et al.*, 1996, *Ryu et al.*, 1996, *Spencer and Jensen*, 1997, *Olson et al.*, 1998a, *Wilkin and Jensen*, 1997b,a, *van Otterlo et al.*, 1998, *Kohandel and Kardar*, 1999). Here, we follow this approach and use Langevin dynamics to study the static and dynamic behaviour of vortices.

Parts of this work are applicable to particle simulations in general and not limited to vortex state simulations. Therefore, we frequently use the term "particle" instead of "vortex".

In addition to the methods described above, there are other approaches to simulate the physics of the vortex state. These range from xy-models (for example *Li and Teitel*, 1994, *Nguyen and Sudbø*, 1999) to the solving of a coarse grained equation of motion for the displacement field

(*Aranson et al.*, 1998), investigating a disordered array of Josephson junctions (for example *Domínguez*, 1999), mapping vortex lines to bosons (for example *Nordborg and Blatter*, 1997) and combination of methods, such as the London-Langevin method coupled to solving the time-dependent Ginzburg-Landau equation (*Bou-Diab et al.*, 2001).

2.3 Equation of motion

The terms in the equation of motion that influence the behaviour of each vortex are the viscous force and a stochastic term from the Langevin equation (2.4), the vortex-vortex interaction, the Lorentz force, and pinning forces. Each of these will be presented in detail in the following subsections.

2.3.1 Overdamped Langevin dynamics

The Langevin dynamics as introduced in section 2.1 form the physical basis of this simulation. The flux motion is strongly overdamped since the viscous force is much greater than any possible inertial forces (*Brandt*, 1995, Sec. 5.2) and the vortex mass can be ignored. The mass term m_i on the left-hand side of equation (2.4) is set to zero and the remaining Langevin equation for vortex i reads (with $\boldsymbol{\chi}_i = \mathbf{F}_i^{\text{thermal}}$):

$$0 = -\eta \dot{\mathbf{r}}_i(t) + \mathbf{F}_i^{\text{vv-interaction}}\left(\mathbf{r}_1(t), \ldots, \mathbf{r}_N(t)\right) + \mathbf{F}^{\text{drive}}(t) + \mathbf{F}_i^{\text{thermal}}(t) + \mathbf{F}^{\text{pinning}}(\mathbf{r}_i(t)). \quad (2.5)$$

The terms represent from left to right: the viscosity term, the forces from the vortex-vortex interaction, the drive or Lorentz force acting on all vortices equally, the noise term which introduces temperature, and the pinning force which depends on the position of the vortex.

2.3.2 Viscosity

The viscosity, η, of the vortex state is related to the Bardeen-Stephen expression for flux-flow resistivity in a homogeneous material (see section 1.3.1 on page 9). The viscous drag coefficient per volume is

$$\eta_{\text{volume}} \approx \frac{B B_{c2}}{\rho_n}. \quad (2.6)$$

Considering that the magnetic induction, B, is represented by N vortices, each carrying a flux quantum Φ_0 over the area A, leads to $B = N\Phi_0/A$. Equation (2.6) can be converted into the viscosity per vortex per unit length $\eta^1_{\text{length}} = \frac{\eta_{\text{volume}}}{N} A \approx \frac{\Phi_0 B_{c2}}{\rho_n}$. The viscosity η in equation (2.5) is given by the viscosity per (pancake) vortex which for a (pancake) vortex of length s is

$$\eta = \eta^1_{\text{length}} s = \frac{\Phi_0 B_{c2}}{\rho_n} s. \quad (2.7)$$

2.3.3 Vortex-vortex interaction

The energy U and force F per unit length of interacting stiff vortex lines separated by a distance r is (see section 1.3.3)

$$U_{\text{line}}(r) = 2\epsilon_0 K_0\left(\frac{r}{\lambda}\right) \qquad \Longleftrightarrow \qquad F_{\text{line}}(r) = \frac{2\epsilon_0}{\lambda} K_1\left(\frac{r}{\lambda}\right) \quad (2.8)$$

and the interaction energy and force between pancakes in the same layer is effectively (*Clem*, 1991)

$$U_{\text{pancake}}(r) = 2\epsilon_0 s \ln\left(\frac{\lambda}{r}\right) \qquad \Longleftrightarrow \qquad F_{\text{pancake}}(r) = \frac{2s\epsilon_0}{\lambda}\frac{1}{r} \quad (2.9)$$

where $\epsilon_0 = \frac{\Phi_0}{4\pi\mu_0\lambda^2}$, λ is the London penetration depth, and s is the layer separation.

For simulations of isolated thin-films, the vortex-vortex interaction is given by Pearl's solution (1.3).

We have implemented all three relevant interactions ($\ln, K_0$ and Pearl's solution), and the interaction potential can be chosen in the configuration file (section 2.10.2.1). We use the smooth cut-off as described in chapter 3 to overcome problems resulting from truncating the interaction.

Using, for example the logarithmic interaction potential (2.9), the vortex-vortex interaction force $\mathbf{F}_{ij}^{\mathrm{vv}}$ felt by pancake i from pancake j at positions $\mathbf{r}_i$ and $\mathbf{r}_j$, respectively, reads

$$\mathbf{F}_{ij}^{\mathrm{vv}}(\mathbf{r}_i - \mathbf{r}_j) = 2\epsilon_0 s \frac{1}{|\mathbf{r}_i - \mathbf{r}_j|} \frac{\mathbf{r}_i - \mathbf{r}_j}{|\mathbf{r}_i - \mathbf{r}_j|} = 2\epsilon_0 s \frac{\mathbf{r}_i - \mathbf{r}_j}{|\mathbf{r}_i - \mathbf{r}_j|^2}, \qquad i \neq j. \tag{2.10}$$

Antisymmetry of $\mathbf{F}^{\mathrm{vv}}$ can be used to optimise its computation. The total force acting on pancake i is given by

$$\mathbf{F}_i^{\mathrm{vv-interaction}} = \sum_{\substack{j=1 \\ j\neq i}}^{N} \mathbf{F}_{ij}^{\mathrm{vv}}(\mathbf{r}_i - \mathbf{r}_j). \tag{2.11}$$

For practical computation, the chosen boundary conditions and a cut-off must be taken into account, as explained in section 2.6.

2.3.4 Lorentz force

The Lorentz force per unit length $\mathbf{f}_{\mathrm{L}} = \mathbf{j} \times \mathbf{\Phi}_0$ acts equally on every vortex (assuming a homogeneous current density). Symbols are as in equation (1.1). The Lorentz force acting on vortices of length s is given by

$$\mathbf{F}^{\mathrm{drive}}(t) = s\, \mathbf{j} \times \mathbf{\Phi}_0. \tag{2.12}$$

2.3.5 Temperature

The thermal motion of a particle i in equilibrium overdamped Langevin dynamics (section 2.3.1) described by

$$0 = -\eta \dot{\mathbf{r}}_{\mathbf{i}} + \zeta_i(t) \tag{2.13}$$

is given by a stochastic noise term which, for clarity, is here called $\zeta_i(t)$ to distinguish it from $\chi_i(t)$ which is used in the simulation. $\zeta_i(t)$ must be normally distributed and have the properties (*Chaikin and Lubensky*, 1995, p.381)

$$< \zeta_i(t) > \; = \; 0 \tag{2.14}$$

and

$$< \zeta_i(t)\zeta_j(t') > \; = \; 2\eta k_{\mathrm{B}} T \delta_{ij} \delta(t - t') \tag{2.15}$$

where η is the viscosity as in equation (2.13), k_{B} the Boltzmann number and T the effective temperature in Kelvin. The angular brackets indicate time-averages in the context of Langevin simulations. Thus, the average of the force from the noise term acting on each particle is zero, and it is neither correlated in time, nor for different particles.

The noise term, χ, chosen in the simulation is

$$\chi(t) = \sigma \Psi \tag{2.16}$$

where $\Psi(t)$ is normally distributed with variance 1.0 with σ as a measure of temperature. It follows that

$$< \chi^2 > = \sigma^2. \tag{2.17}$$

To relate σ to the effective temperature, T, one has to consider that the differential equation of motion is solved discretised in time. This means that high-frequency components of the stochastic term, $\zeta(t)$, are ignored and that $\chi(n\Delta t)$, $n \in \mathbb{N}$, represents the average of $\zeta(t)$ over a time step Δt. Therefore, one has to consider the correlations of the impulses rather than the forces ζ and χ:

$$\begin{aligned}
\left\langle \int_t^{t+\Delta t} \int_{t'}^{t'+\Delta t} \zeta(t)\zeta(t')\mathrm{d}t\mathrm{d}t' \right\rangle &= \int_t^{t+\Delta t} \int_{t'}^{t'+\Delta t} < \zeta(t)\zeta(t') > \mathrm{d}t\mathrm{d}t' \\
&\overset{(2.15)}{=} \int_t^{t+\Delta t} \int_{t'}^{t'+\Delta t} 2\eta k_\mathrm{B} T \delta(t-t')\mathrm{d}t\mathrm{d}t' \\
&= 2\eta k_\mathrm{B} T \int_t^{t+\Delta t} \mathrm{d}t \quad = \quad 2\eta k_\mathrm{B} T \Delta t
\end{aligned} \tag{2.18}$$

and for χ we obtain $\left\langle \int_t^{t+\Delta t} \int_{t'}^{t'+\Delta t} \chi^2 \mathrm{d}t\mathrm{d}t' \right\rangle \overset{(2.17)}{=} \sigma^2 (\Delta t)^2$. Now the last two expressions can be equated to relate the effective temperature, T, to the temperature parameter, σ, in the simulation:

$$T = \frac{\Delta t}{2\eta k_\mathrm{B}} \sigma^2. \tag{2.19}$$

We will later express forces in multiples of $f_0 \overset{(2.29)}{=} 2\epsilon_0 s / L_\mathrm{scale}$ and the time-step Δt in units of $t_\mathrm{scale} \overset{(2.32)}{=} L_\mathrm{scale}\eta / f_0$ and denote dimensionless parameters with a tilde (section 2.7). Eventually we use $\sigma = \sqrt{\tilde{T}} f_0$ where $\tilde{T}$ is the dimensionless temperature parameter in the simulation, and relates to the real temperature, T, via

$$T = \frac{\Delta t f_0^2}{2\eta k_\mathrm{B}} \tilde{T} = \frac{t_\mathrm{scale} \widetilde{\Delta t} f_0^2}{2\eta k_\mathrm{B}} \tilde{T} \overset{(2.32)}{=} \frac{\widetilde{\Delta t} L_\mathrm{scale} f_0}{2 k_\mathrm{B}} \tilde{T} \overset{(2.29)}{=} \frac{\epsilon_0 s \widetilde{\Delta t}}{k_\mathrm{B}} \tilde{T}. \tag{2.20}$$

2.3.6 Pinning

The values of the pinning potential are stored on a fine two-dimensional grid, and we interpolate to obtain potential values between the grid-points.

2.3.6.1 Pinning interpolation methods

In this section we describe technical details of this interpolation, and have chosen a point like pin on a very coarse grid for demonstration purposes.

To compute potential values between the grid-points, we use either a bi-linear or a bi-cubic interpolation method. The bi-cubic method results in a smoother potential. We demonstrate this in figure 2.2.

In figure 2.3 we show a one-dimensional cut through a pinning potential. On the left plot, we demonstrate the difference between the two interpolation techniques for an even coarser pinning potential. It can be seen that the cubic method results in a smooth line, but overshoots. The right plot shows a problem that can occur from using linear interpolation: a trapped particle may oscillate artificially around its equilibrium position.

The overshooting of the cubic interpolation is due to the discontinuity of the first derivative at $x = \pm 0.5$, and this problem is unlikely to happen for realistic pinning potentials: the vortex

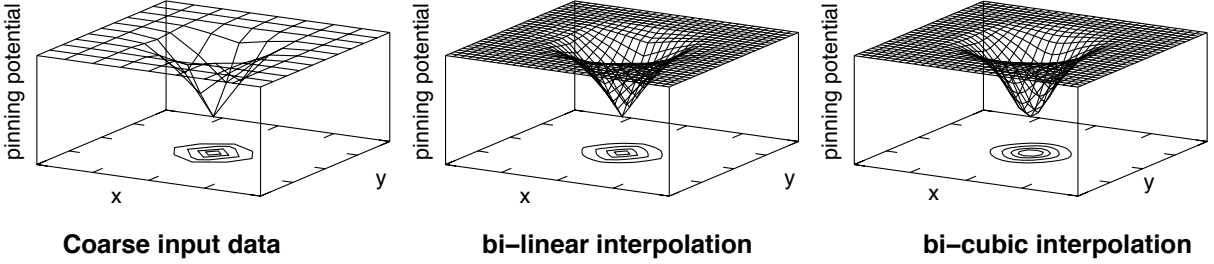

Figure 2.2: Demonstration of pinning potential interpolation. *Left:* Original pinning data as stored in file, showing $-\exp(-r^2)$. For demonstration purposes we have chosen the mesh to be very coarse in order to better visualise the interpolation process. For intermediate positions we interpolate the pinning data. *Middle:* Bi-linear interpolation. *Right:* Bi-cubic interpolation.

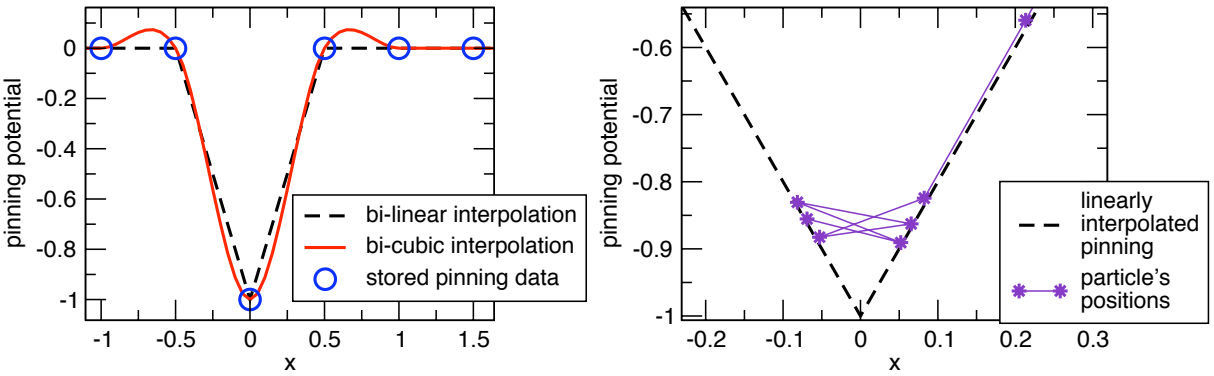

Figure 2.3: *Left:* Comparison of linear interpolation (dashed line) and cubic interpolation (solid line) between the defined potential values (circles). The cubic interpolation results in a smooth minimum at $x = 0$, but overshoots, for example, at $0.5 < x < 1$ thus creating an artifical barrier. *Right:* Bi-linear interpolation of the pinning potential. Artificial behaviour can occur on a small scale: Suppose a particle drops into a pinning well, which is as crudely approximated as shown here. In the absence of other forces it will oscillate around the minimum in the pinning potential.

core smears pinning over a length scale ξ and the pinning potential should reflect this and therefore vary smoothly. Therefore, the cubic interpolation is the safe method to describe a smoothly varying pinning potential, but for sufficiently fine pinning meshes, the linear interpolation produces the same results.

2.3.6.2 Different pinning types

Apart from using the well known-point like pinning (top in figure 2.5), one can employ a random pinning potential that varies smoothly on a length scale of $\lambda/25$, which is of the order of the coherence length ξ. This is a representation of random pinning on the atomic length scale (for example due to oxygen vacancies or small clusters of oxygen vacancies) since the vortex cores effectively smooth the pinning potential over a length scale of the core diameter 2ξ. Figure 2.4 (a) demonstrates the construction of the pinning potential in one dimension. Figure 2.4 (b) shows a part of the pinning structure used for the two dimensional system. The root mean square value of the corresponding pinning forces is denoted by $F_{\mathrm{rms}}^{\mathrm{vp}}$.

This choice of the pinning potential is more realistic for high-quality single crystal samples

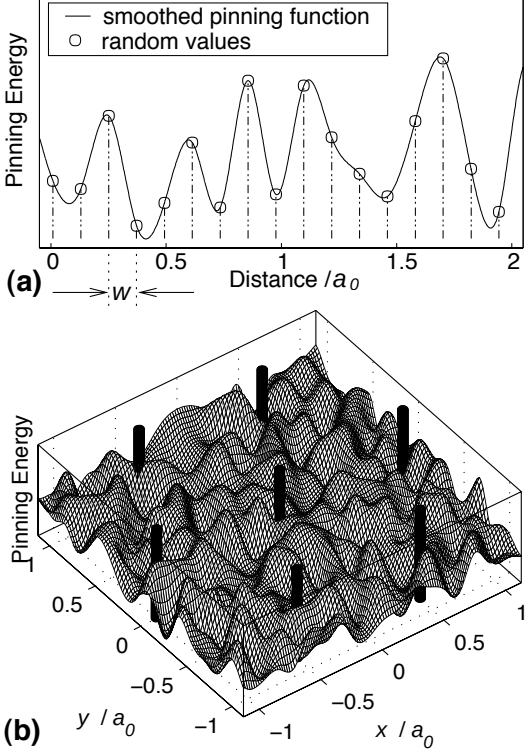

Figure 2.4: A sample pinning potential. Distances are given in multiples of the vortex lattice spacing, a_0. *(a)* Demonstration of construction of the pinning potential in one dimension: firstly, we assign random pinning energies at discrete sites (shown as open circles) with spacing w. Secondly, we interpolate between those sites using cubic splines to obtain an effectively continuous pinning potential. This results in a random pinning potential with a short-range correlator $\overline{V(r)V(r')} = g(r - r')$ of range w. We follow an analogous procedure in two dimensions. *(b)* A part of a pinning potential as used in the simulations. The seven black cylinders indicate vortex lines separated by a_0 to demonstrate the length scale.

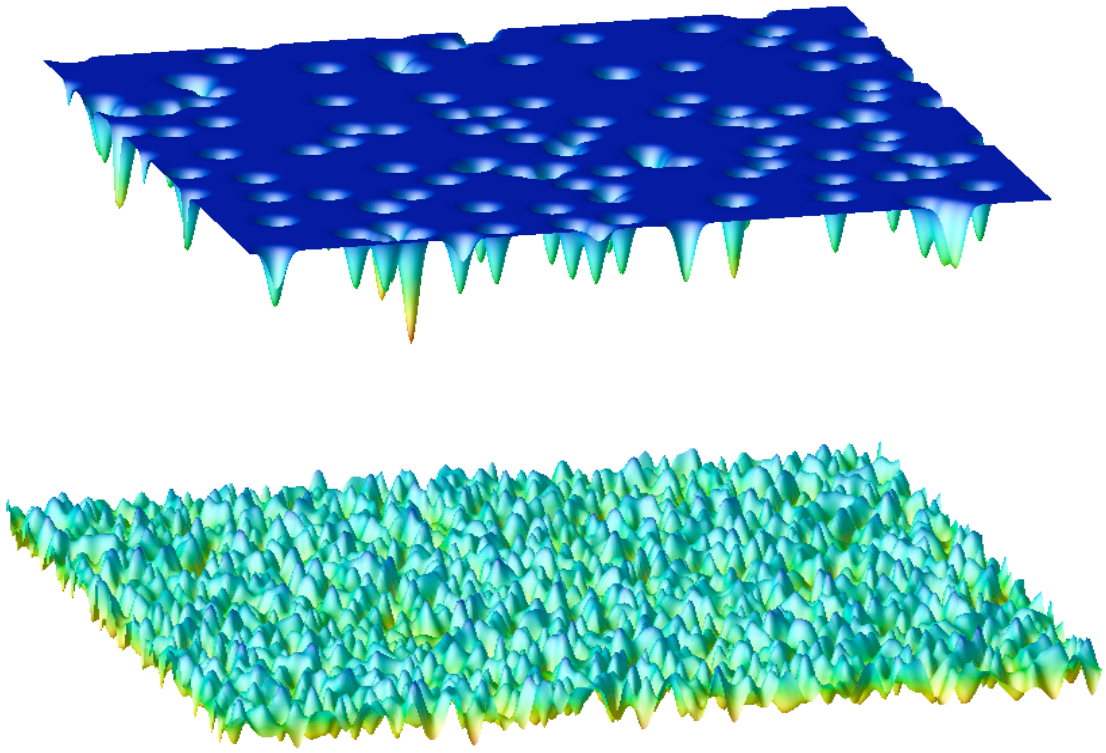

Figure 2.5: Comparison of different pinning potentials. *Top:* Point-like pinning centres as employed by most other simulations of the vortex state. Parameters taken from *Olson et al.* (1998b), *Olson and Reichhardt* (2000). *Bottom:* Smoothly varying pinning potential as used in this work. Both plots show an area which is occupied by ≈ 90 vortices.

than the pinning of few, relatively strong point-like pinning centres. We demonstrate the different shapes of the pinning potential in figure 2.5.

2.3.6.3 Computing the pinning force, and measuring pinning strength

To obtain the force $\mathbf{F}^{\text{pinning}}(\mathbf{r}_i(t))$ for vortex i at position $\mathbf{r}_i(t)$ one needs the negative gradient of the pinning potential which we compute numerically. We measure the strength of a pinning potential by the root-mean-square value of its force

$$F_{\text{rms}}^{\text{vp}} = \left(\int \mathrm{d}^2 r \quad |\mathbf{F}^{\text{vp}}(\mathbf{r})|^2 \right)^{\frac{1}{2}}. \tag{2.21}$$

2.4 Random pinning

2.4.1 The complete equation of motion

Having considered all the forces contributing to the equation of motion, one obtains the following system of N two-dimensional first order ordinary differential equations which describes the motion of vortex pancakes with time in one layer:

$$\begin{aligned} \eta \dot{\mathbf{r}}_i(t) &= \mathbf{F}_i^{\text{vv-interaction}}(\mathbf{r}_1(t), \ldots, \mathbf{r}_N(t)) + \mathbf{F}^{\text{drive}}(t) + \mathbf{F}_i^{\text{thermal}}(t) + \mathbf{F}^{\text{pinning}}(\mathbf{r}_i(t)) \\ &= 2\epsilon_0 s \sum_{\substack{j=1 \\ j \neq i}}^{N} \frac{\mathbf{r}_i(t) - \mathbf{r}_j(t)}{|\mathbf{r}_i(t) - \mathbf{r}_j(t)|^2} + s \cdot \mathbf{j}(t) \times \mathbf{\Phi_0} + \mathbf{F}_i^{\text{thermal}}(t) + \mathbf{F}^{\text{pinning}}(\mathbf{r}_i(t)) \\ & \quad i = 1, \ldots, N \qquad \text{and} \qquad (\mathbf{r}_1(t_0), \mathbf{r}_2(t_0), \ldots, \mathbf{r}_N(t_0)) = (\mathbf{r}_1^0, \mathbf{r}_2^0, \ldots, \mathbf{r}_N^0) \end{aligned} \tag{2.22}$$

The constants η and ϵ_0 are defined in equations (2.7) and (1.4), respectively, s is the length of a vortex, $\mathbf{j}$ is the current density of the transport current, $\mathbf{\Phi}_0$ is the flux quantum directed along the magnetic field perpendicular to the layer, and the $\mathbf{r}_i^0$ are the initial positions of the pancakes at time $t = t_0$.

2.5 Solving the equation of motion

The problem to be solved as given in equation (2.22) is an initial value problem for a coupled set of $2N$ ordinary first order differential equations. Each equation can be written as

$$\frac{\mathrm{d}x}{\mathrm{d}t}(t) = f(t, x) \qquad \text{with} \qquad x(t_0) = x_0. \tag{2.23}$$

Integrating equation (2.23) from time t_n to time t_{n+1} yields

$$x(t_{n+1}) = x(t_n) + \int_{t_n}^{t_{n+1}} f(t, x(t))\, \mathrm{d}t. \tag{2.24}$$

This converts the problem into solving an integral. Integration methods with varying step size $\Delta t = t_{n+1} - t_n$ cannot be used, because a changing step size would change the effective temperature, as visible in equation (2.19).

In principle, there are a variety of methods available to integrate equation (2.24). Most of them can quickly be dismissed for the reason that the most expensive part of the computation is

the evaluation of the right-hand side of equation (2.24). Therefore, any method requiring more than one such calculation per time step is wasteful, unless it can deliver a proportionate increase in the step size Δt. However, due to the strongly repulsive force for vortices approaching each other closely, there is an effective upper bound for Δt (*Rapaport*, 1995, p.57).

For this reason, in molecular dynamics simulations only "predictor-corrector" methods or low order "leap-frog" methods play important roles (*Haile*, 1997, p.158). Predictor-corrector methods use information from several previous time steps to approximate the function to integrate by a polynomial, but cannot be used in Langevin simulations as the noise term, $\mathbf{F}^{\text{thermal}}$, in (2.22) introduces discontinuities in the right-hand side of (2.24) and the predictor-corrector method relies on $f(t, x(t))$ being a smooth and continuous function. The typical leap-frog integration employs a simple Euler-integration step for both the velocity and the positions, but computes velocities and positions on a staggered grid in time. The leap-frog method is very stable.

We use a leap-frog type integration scheme which is equivalent to Euler's method since we have no second order derivative in (2.22). For zero-temperature runs, predictor-corrector methods can be employed, but one has to reduce the time step size in comparison to the leap-frog method to make them stable, and the gain in accuracy is not worth the effort: *Rapaport* (1995, p.57) states that a high degree of accuracy in the trajectories is neither a realistic nor a practical goal, and this is particularly true for differential equations with a stochastic term. It is more important that time- and space-dependent correlations can be reproduced. For finite temperatures in our simulations, predictor-corrector methods are intrinsically unstable as they are based on the assumption that the right-hand-side of the differential equation (2.22) can be described by a polynomial. In particular, this requires continuity which is not given with the randomly varying Langevin noise term.

2.6 Boundary conditions

One simple form of boundary conditions are "hard" boundary conditions: we confine the vortices inside the simulation cell and do not to allow them to cross the boundary. Results of such a run starting from a hexagonal vortex distribution are shown in figure 2.6. The hexagonal configuration is unstable, and the majority of vortices moves to the borders because there is no repulsion from outside the simulation cell.

We are generally interested in the case where the vortex density stays approximately constant. In particular, we would like the hexagonal configuration to be the ground state and therefore stable. This is easily achieved by the conventional approach of using periodic boundary conditions, (next section 2.6.1).

2.6.1 Periodic boundary conditions

The standard approach in particle simulations in order to avoid the influence of surfaces on the system is to use periodic boundary conditions (for example *Rapaport*, 1995, p.16). A system of infinite size is simulated by tiling space with an infinite array of identical copies of the finite simulation region, as indicated in figure 2.7 for only eight copies. There are two different approaches how to deal with particle-particle interactions across the border of the simulation cell:

- The cut-off method cuts off the interaction at some distance shorter than half the length of the simulation cell. This avoids self-interaction of particles. For long-range forces this

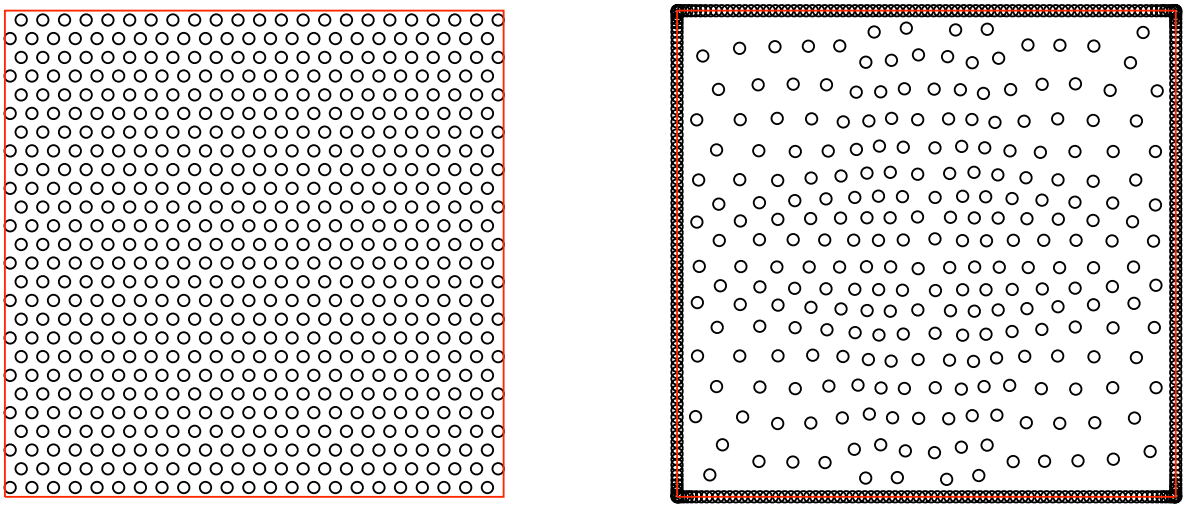

Figure 2.6: *Left:* Initial hexagonal vortex configuration. *Right:* Final configuration after relaxation from configuration shown on the left, using hard boundaries. Due to the strong repulsion, vortices gather at the boundary and the vortex distribution is spatially inhomogeneous. Note, that the apparent thick line around the simulation cell is in fact composed of overlapping circles which represent the vortices at the system's boundary.

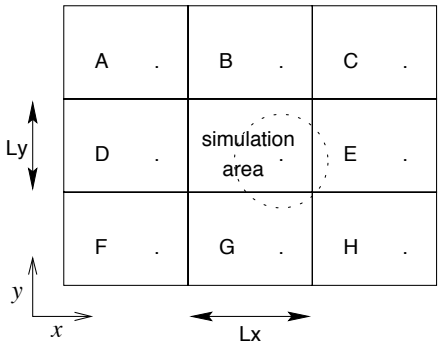

Figure 2.7: Periodic boundary conditions within the planes. The primary cell is surrounded by eight image cells (A to H) of itself. One vortex and all its mirror images are drawn in the lower right corner of the simulation area. Also, the cut-off range for the computation of the interaction force of this vortex with all other vortices is indicated by the dotted circle.

approach can give misleading results (see chapter 3).

- The infinite lattice summation takes into account the interaction of the particles with all particles in all infinite repeats of the simulation cell in order to evaluate forces and energies. Every particle interacts with all its mirror images which is only feasible if the infinite double sum can be simplified. This method can impose an artificial periodicity onto the system, and is usually computationally more complex than the cut-off approach.

Both methods will be discussed in detail in chapter 3, where we demonstrate that long-range potentials have to be cut-off smoothly, and where we derive a fast method to compute an infinite lattice summation for particles interaction with the Bessel function potential $K_0(\mathbf{r})$. In addition, we have implemented the infinite lattice summation for logarithmic interaction which was developed by *Grønbech-Jensen* in 1996.

In principle, any space-filling convex region can be used as the shape of the primary cell. We have chosen a rectangular simulation cell with lengths L_x and L_y being commensurate with a hexagonal lattice to avoid frustration of the system. Other shapes can be used, but provide no advantage (section 3.3).

2.7 Simulation units

It is advisable to scale variables in the simulation such that resulting numbers are of the order of unity: firstly, numerical overflow and underflow have to be avoided. Secondly, scaling can simplify tracking down errors because humans are better in working with number of the order of unity rather than big or small numbers that have to be expressed with exponents. Finally, universal parameters can be identified: it may turn out (by investigating the equations) that some parameters of the problem are irrelevant for the computation, and that numerical results can be scaled afterwards with these parameters.

We label quantities expressed in dimensionless simulation units with a tilde, and introduce scaling factors L_{scale} for length and t_{scale} for time such that

$$\mathbf{r} = L_{\text{scale}}\tilde{\mathbf{r}} \qquad \text{and} \qquad t = t_{\text{scale}}\tilde{t}. \tag{2.25}$$

We express equation (2.22) schematically as

$$\frac{\mathrm{d}\mathbf{r}_i}{\mathrm{d}t} = \mathbf{v}_i = \frac{1}{\eta}(\mathbf{F}_i^{\text{vv-interaction}} + \mathbf{F}_i^{\text{pinning}} + \mathbf{F}_i^{\text{thermal}} + \mathbf{F}^{\text{drive}}) \tag{2.26}$$

with ($\mathbf{r}_{ij}$ representing the displacement of vortex j from vortex i, and $r_{ij} = |\mathbf{r}_{ij}|$)

$$\mathbf{F}_i^{\text{vv-interaction}} \overset{(2.11)}{=} \sum_{j\neq i} \mathbf{F}_{ij}^{\text{vv}}(\mathbf{r}_{ij}) \overset{(2.10)}{=} \sum_{j\neq i} 2\epsilon_0 s \frac{1}{r_{ij}}\frac{\mathbf{r}_{ij}}{r_{ij}}. \tag{2.27}$$

We introduce the scaling length L_{scale} into $\mathbf{F}_{ij}^{\text{vv}}$ given in (2.10)

$$\mathbf{F}_{ij}^{\text{vv}}(\mathbf{r}_{ij}) = 2\epsilon_0 s \frac{1}{r_{ij}}\frac{\mathbf{r}_{ij}}{r_{ij}} = \frac{2\epsilon_0 s}{L_{\text{scale}}}\frac{1}{\tilde{r}_{ij}}\frac{\tilde{\mathbf{r}}_{ij}}{\tilde{r}_{ij}} \equiv f_0 \tilde{r}_{ij}\frac{\tilde{\mathbf{r}}_{ij}}{\tilde{r}_{ij}} = f_0 \tilde{\mathbf{F}}_{ij}^{\text{vv}}(\tilde{\mathbf{r}}_{ij}) \tag{2.28}$$

which defines our unit of force, f_0, as the repulsion two vortices experience when they are separated by L_{scale}:

$$f_0 = |\mathbf{F}_{ij}^{\text{vv}}(L_{\text{scale}})| = \frac{2\epsilon_0 s}{L_{\text{scale}}} \overset{(1.4)}{=} \frac{\Phi_0^2 s}{2\pi\mu_0\lambda^2 L_{\text{scale}}}. \tag{2.29}$$

Using

$$\mathbf{v}_i = \frac{\mathrm{d}\mathbf{r}_i}{\mathrm{d}t} = \frac{L_{\text{scale}}}{t_{\text{scale}}}\frac{\mathrm{d}\tilde{\mathbf{r}}_i}{\mathrm{d}\tilde{t}} = \frac{L_{\text{scale}}}{t_{\text{scale}}}\tilde{\mathbf{v}}_i \tag{2.30}$$

we rewrite (2.26) as

$$\frac{\mathrm{d}\tilde{\mathbf{r}}_i}{\mathrm{d}\tilde{t}} = \tilde{\mathbf{v}}_i = \frac{t_{\text{scale}}}{L_{\text{scale}}}\frac{f_0}{\eta}\left(\tilde{\mathbf{F}}_i^{\text{vv-interaction}} + \tilde{\mathbf{F}}_i^{\text{pinning}} + \tilde{\mathbf{F}}_i^{\text{thermal}} + \tilde{\mathbf{F}}^{\text{drive}}\right). \tag{2.31}$$

We fix the time-scale t_{scale} by requiring

$$\frac{t_{\text{scale}}}{L_{\text{scale}}}\frac{f_0}{\eta} = 1 \qquad \Longleftrightarrow \qquad t_{\text{scale}} = \frac{L_{\text{scale}}\eta}{f_0}. \tag{2.32}$$

We choose

$$L_{\text{scale}} = \lambda \tag{2.33}$$

parameter	symbol	comment	approx. value
YBCO:			
anisotropy	Γ_a		5 - 7
penetration depth (parallel to layers)	λ		1400Å
coherence length	ξ		15Å
layer spacing	s		12Å
upper critical field	B_{c2}	at $T = 90$K	6T
superconductivity transition	T_c	at $B = 0$T	93K
normal state resistivity	ρ_n		$10^{-6}\Omega$m
pancake viscosity (2.7)	η		$1.4 \cdot 10^{-17}$kg/s
BSCCO:			
anisotropy	Γ_a		50-200
penetration depth parallel to layers	λ		$1400 - 2000$Å
coherence length	ξ		$20 - 40$Å
layer spacing	s		15Å
superconductivity transition	T_c	at $B = 0$T	110K
Other entities:			
Planck's constant	h	$2\pi\hbar$	$6.6 \cdot 10^{-34}$Js
electron charge	e		$1.6 \cdot 10^{-19}$C
flux quantum	Φ_0	$\frac{h}{2e}$	$2.1 \cdot 10^{-15}$Tm^2
vacuum permeability	μ_0		$4\pi 10^{-7} \frac{\text{Vs}}{\text{Am}}$
vortex lattice spacing	a_0	$a_0 = \sqrt{\frac{2\Phi_0}{\sqrt{3}B}}$	at $B = 1$T: $a_0 \approx 500$Å

Table 2.1: Typical values for $YBa_2Cu_3O_{7-\delta}$ and $Bi_2Sr_2CaCu_2O_8$ compounds (*Blatter et al.*, 1994, *Tinkham*, 1996, *Gordeev*, 2000) and some physical constants.

name	relation	factor	typical value (YBCO)
Scaling factors			
length (2.33)	$r = L_{\text{scale}}\tilde{r}$	$L_{\text{scale}} = \lambda$	1400Å
time (2.32)	$t = t_{\text{scale}}\tilde{t}$	$t_{\text{scale}} = \frac{L_{\text{scale}}\eta}{f_0}$	$9.1 \cdot 10^{-12}$s
velocity	$v = \frac{L_{\text{scale}}}{t_{\text{scale}}}\tilde{v}$	$\frac{L_{\text{scale}}}{t_{\text{scale}}} = \frac{f_0}{\eta}$	$1.5 \cdot 10^{4}$m/s
force (2.29)	$F = f_0\tilde{F}$	$f_0 = \frac{2\epsilon_0 s}{\lambda}$	$2.2 \cdot 10^{-13}$N
energy	$E = e_0\tilde{E}$	$e_0 = L_{\text{scale}} f_0 = 2\epsilon_o s$	$3 \cdot 10^{-20}$Nm ≈ 0.2eV
temperature (2.20)	$T = T_0\tilde{T}$	$T_0 = \frac{\Delta t f_0^2}{2\eta k_{\text{B}}} = \frac{\epsilon_0 s \widetilde{\Delta t}}{k_{\text{B}}}$	5.6K
Gamma: $\Gamma \equiv \frac{k_{\text{B}}T}{2\epsilon_0 s}$	$\Gamma = \frac{\Gamma_0}{\tilde{T}}$	$\Gamma_0 = \frac{2}{\widetilde{\Delta t}}$	400
Other factors			
ϵ_0 (1.4)		$\epsilon_0 = \frac{\Phi_0^2}{4\pi\mu_0\lambda^2}$	$1.3 \cdot 10^{-11}$N
time step $\widetilde{\Delta t}$			0.005

Table 2.2: Typical values for simulation scaling factors using physical parameters given in table 2.1, and some other factors used. See equation 1 in *Fangohr et al.* (2002) for the definition and use of Γ.

but any length of the order of the vortex-spacing would suffice. We thus get a dimensionless equation of motion in which all terms are of the order of unity:

$$\frac{\mathrm{d}\tilde{\mathbf{r}}_i}{\mathrm{d}\tilde{t}} = \tilde{\mathbf{F}}_i^{\text{vv-interaction}} + \tilde{\mathbf{F}}_i^{\text{pinning}} + \tilde{\mathbf{F}}_i^{\text{thermal}} + \tilde{\mathbf{F}}^{\text{drive}}. \tag{2.34}$$

Table 2.1 shows some typical values for $YBa_2Cu_3O_{7-\delta}$ materials, and table 2.2 shows the resulting scaling factors for a simulation using those values. Our choice for the scaling parameters and the resulting natural length, L_{scale}, and time, t_{scale}, are in line with other simulations (*Ryu et al.*, 1996, *van Otterlo et al.*, 1998).

2.7.1 Smallness of time step

The time scale of the simulation is given by t_{scale}. It turns out that for a typical field $B = 1$T, a time step of $\Delta t \leq 0.005\, t_{\text{scale}}$ has to be used to obtain accurate and stable solutions of the system of differential equations in equation (2.34). This is due to the diverging repulsive vortex-vortex interaction term. If the step size is too large, then vortices come too close to each other and will shoot off in the next time step because they feel a large repulsive force. The smallness of the time step (in real units about 0.5 picoseconds) is, in fact, a common feature of molecular dynamics simulations of microscopic systems (*Allen and Tildesley*, 1989, p.155, and *Haile*, 1997, p.163). This limits quantitative simulations to time scales $\approx 0.1\mu$s, since about one million time steps can be computed in reasonable time (for $B = 1$T).

The main problem in quantitative high-temperature superconductor simulations of the vortex state is that the critical Lorentz force, F_c, required to depin the system can be very small, for example in comparison to the force $F_{j_0}^{\text{drive}}$ exerted by the Cooper-pair depairing current $j_0 = \Phi_0/(3\sqrt{3}\pi\lambda_{ab}^2\xi\mu_0) \approx 3 \cdot 10^{12}\text{Am}^{-2}$ (*Brandt*, 1995, Sec 1.1). Whereas at low temperatures for YBCO the ratio $F_c/F_{j_0}^{\text{drive}}$ is of the order of $j_c/j_0 \approx 0.01$ (*Higgins and Bhattacharya*, 1996), it becomes much smaller for larger temperatures. At liquid nitrogen temperature the depinning current density is of the order $j = 10^5\text{Am}^{-2}$ corresponding to $F_c/F_{j_0}^{\text{drive}} \approx 3 \cdot 10^{-8}$. For a driving

force $F^{\text{drive}} = 3 \cdot 10^{-6} F_{j_0}^{\text{drive}}$ the resulting free flow velocity is so small that the vortex system travels less than one lattice spacing a_0 within 0.1μs.

In simulation units the de-pairing drive is[2] $\tilde{F}_{j_0}^{\text{drive}} \approx 30$. The smallest (transverse) forces investigated in this work are of the order of $10^{-4} f_0$ and the largest forces are $8 f_0$ corresponding to $3 \cdot 10^{-6} \tilde{F}_{j_0}^{\text{drive}}$ and $\approx 0.25 \tilde{F}_{j_0}^{\text{drive}}$, respectively.

In computer simulations of the vortex state, Lorentz forces which are significantly larger than realistic for high temperatures are employed to compensate for the smallness of the time interval (for example *Olson et al.*, 1998a, *van Otterlo et al.*, 1998). Accordingly, there is a tendency to choose the strength of the pinning potential to be too big to allow investigation of the depinning transition.

In other areas of research using molecular dynamics techniques similar problems exist. Two examples are simulations of protein unfolding, in which unphysically high temperatures are used to trigger the reaction to happen within the simulation time window (*Tirado-Rives and Jorgensen*, 1993), and computations which model the stretching of a dextran molecule due to an atomic force microscope (AFM), in which the simulated pulling force used is nine orders of magnitude larger than in the experiment (*Rademacher*, 1999).

In summary, whereas the low-temperature regime can be simulated with quantitatively reasonable parameters, this is not possible for the dynamics in the high-temperature regime. This is due to the small time window a computer simulation can cover.

2.8 Limits of model applicability

The described simulation is a model of a set of classical repelling massless point-like particles under the influence of thermal fluctuations, a driving force, and an underlying potential in two dimensions. This can be related to the vortex state in high-temperature superconductors in two-dimensional (thin-films, stack of superconducting layers) and quasi-two-dimensional systems (rigid vortices) with and without pinning, and at zero and finite temperatures. Using the substrate model (*Fangohr et al.*, 2002) we can also study a three-dimensional layered system in the high anisotropy limit of zero Josephson coupling with electromagnetic interlayer interactions. Our simulation can also be related to the classical two-dimensional one-component plasma (*de Leeuw and Perram*, 1982, *Caillol et al.*, 1982, *Choquard*, 1983) in which electrons experience the same logarithmic repulsion. In the context of the vortex state we mention two limitations:

- The use of classical particles to represent vortices makes it impossible to include phenomena such as vortex-anti-vortex pair creations. Of course, the breakdown of superconductivity at too high a field or too high a temperature cannot be simulated either. Therefore, the simulation should not be applied to regimes near the upper or lower critical field.

- Quantitative simulations of dynamic systems are restricted by the smallness of the time scale that can be simulated (subsection 2.7.1). However, the number of computer simulations being subjected to the same or similar restrictions and still providing great insight into physical concepts encourages the belief that the results are qualitatively correct, even if driving forces which are artificially large have to be used.

[2] $\tilde{F}_{j_0}^{\text{drive}} = F_{j_0}^{\text{drive}} / f_0 \overset{(2.12)}{=} |\mathbf{j}_0 \times \mathbf{\Phi_0} s| / f_0 = \ldots = 2L_{\text{scale}} / (3\sqrt{3}\xi)$

2.9 Observables

2.9.1 Positions and velocities

The governing equation of motion (2.22) automatically provides velocities and positions of all vortices as a function of time, and we can compute the "centre of mass"-position and velocity of the system

$$\mathbf{r}_{\mathrm{cm}}(t) = \frac{1}{N}\sum_{i=1}^{N}\mathbf{r}_i(t) \qquad \text{and} \qquad \dot{\mathbf{r}}_{\mathrm{cm}}(t) = \frac{1}{N}\sum_{i=1}^{N}\dot{\mathbf{r}}_i(t). \tag{2.35}$$

Periodic boundary conditions are considered in the computation of the centre of mass, *i.e.* a vortex leaving the simulation box to the left and re-entering from the right will not result in a discontinuity in $\mathbf{r}_{\mathrm{cm}}(t)$.

2.9.2 Energy

The energy of the system consists of the electromagnetic interaction between vortices (section 1.3.3), and the energy gain from the pinning surface. There is no kinetic energy since the inertial mass is zero.

2.9.3 Mean square displacement

The running mean square displacement

$$\Delta r^2(t) = \frac{1}{N}\sum_{i=1}^{N}[\mathbf{r}_i(t) - \mathbf{r}_i(t_0)]^2 \tag{2.36}$$

can be used to distinguish between a solid and a liquid state of the system. For a solid, $\Delta r^2(t)$ remains nearly constant, whereas for a fluid it increases almost linearly with time (*Haile*, 1997, p.209).

2.9.4 Structure factor

The structure factor as the Fourier transform of the local density $\rho(\mathbf{r}) = \sum_{l=1}^{N}\delta(\mathbf{r}-\mathbf{r}_l)$ for a set of N discrete particles reads

$$S(\mathbf{k}) = \int \mathrm{d}\mathbf{r}\,\sum_{l=1}^{N}\delta(\mathbf{r}-\mathbf{r}_l)\exp(-i\mathbf{k}\cdot\mathbf{r}) = \sum_{k=l}^{N}\exp(-i\mathbf{k}\cdot\mathbf{r}_l). \tag{2.37}$$

This can be evaluated numerically for every required value of $\mathbf{k}$. An alternative approach to compute $S(\mathbf{k})$ for many $\mathbf{k}$, is to define a coarse grained density function $\tilde{\rho}(r)$ based on a two-dimensional grid with suitable spatial resolution and equidistant grid points and then to use a discrete two-dimensional fast Fourier transform (*Frigo and Johnson*, 1998) to obtain $S(\mathbf{k})$. The latter method is more efficient if we require $S(\mathbf{k})$ for many $\mathbf{k}$.

2.9.5 Delaunay triangulation

The Delaunay triangulation for a set of points in a plane can be defined as in *de Berg et al.* (1997, p.188): "A triangulation of a set of points $\mathcal{P}$ is the Delaunay triangulation if and only if the circumcircle of any triangle (going through the three points of the triangle) in the triangulation does not contain any further points of $\mathcal{P}$ in its interior." The Delaunay triangulation is unique,

if points are not co-circular, *i.e.* four particles must not be located on a circle. The Delaunay triangulation allows easy visualisation of the lattice structure of a set of particles and also provides further topological data such as the nearest neighbours.

We have used the "Quickhull"-routine in order to obtain Delaunay triangulations of vortex positions. The source code in C, which has kindly been provided by the Indianapolis Computation Geometry Centre (*Geometry Centre*, 1999), has been integrated in the analysis software. For sets with co-circular points the data is randomly jiggled to resolve this undefined situation. Details of the very efficient algorithm employed, are found in *Barber et al.* (1996).

2.9.6 Number of defects

The Delaunay triangulation provides information about nearest neighbours, and by counting them we find vortices with more or less than six nearest neighbours. These are referred to as topological defects.

2.9.7 Local hexagonal order

From the Delaunay triangulation the bond angles, θ_k, of the vortices can be evaluated. Using these, a parameter Ψ_6 that represents the local hexatic order of the system can be computed:

$$\Psi_6 = \frac{1}{n_{\text{bond}}} \left| \sum_{k=1}^{n_{\text{bond}}} \exp(i6\theta_k) \right| \tag{2.38}$$

Here, n_{bond} gives the number of bonds (or equivalently angles) in the Delaunay triangulation which are considered to be numbered from 1 to n_{bond}. For a perfect hexagonal lattice $\Psi_6 = 1$.

2.9.8 Other observables

A variety of observables can easily be computed in the framework of the substrate model, and equations are given in citetFangohr02a.

2.10 Simulation software

2.10.1 Programming language

We have developed a suite of programs written in platform independent ANSI C++, complemented with a set of Python[3] and Bash[4]-scripts to assist in data analysis and job submission.

2.10.2 A computation cycle

2.10.2.1 Input data

The user specifies their requirements by writing the configuration of a run (run-ID, number of vortices, magnetic induction, vortex-interaction, ...), in a simple text-file, called a *configuration file*. If a pinning potential is required, then the name of a data-file[5] containing the potential is included in the file. Any time-dependent events (such as an increase of the driving force) are including in this configuration file in the form of an event list.

[3] Python is on object oriented, interactive, interpreted language. (`http://www.python.org`)

[4] Bash is the "Bourne again shell" and available for Linux/Unix and windows operating systems.

[5] We have a selection of input formats for pinning potentials, for example a two-dimensional table in plain text, or a bitmap such as a jpeg or png-file.

It is advantageous to have configuration files stored in plain text as they can easily be created and modified by scripts, which is useful for parameter space exploration.

2.10.2.2 Pre-processing of input data

The configuration file is processed by the first program of our suite. This checks for correct syntax and plausibility. If required, further parameters — which usually the user does not need to care about — are computed (such as coefficients for the smoothing of the interaction close to the cut-off), and eventually a *parameter file*, based on the user input *configuration* file, is written by the program. This file contains all information that the simulation software needs to perform the simulation.

There are two reasons for this step: firstly, we check for typos and other mistakes so we can be reasonably sure that the computation based on this parameter file will not fail for trivial reasons. Secondly, having all information in a text file means that by simply storing this file (and the corresponding pinning data), a run can be reproduced. Note also, that no re-compilation is required at any stage because no configuration details are hard-coded.

2.10.2.3 The computation

At the beginning of the computation the parameter file is read, the pinning potential is loaded, and tables (for infinite lattice summations, and pinning interpolation) are precomputed. Then all requested time-steps are computed, and vortex positions are saved to disk regularly.

If requested in the parameter file, the driving force, pinning strength or temperature can change at specified time steps. No user intervention is required to perform the complete computation which is important when running jobs on computational (non-interactive) clusters.

2.10.2.4 Data analysis

A third program operates on the saved data files and allows to extract the raw stored data as well as derived observables. We have provided methods to write data to a variety of formats to be able to use different tools for data analysis. We mainly use OpenDX[6] and Xmgrace[7] to visualise static and dynamic data. For high-quality presentations and animations of the pinning surface, we use PovRay.[8]

2.10.3 Computational infrastructure

We have used the Beowulf cluster of the University of Southampton with 324 CPUs running at 1GHz and 1.5GHz. Jobs are submitted via a queuing system.

2.11 Summary

A model of the vortex state in high-temperature superconductors has been proposed and implemented efficiently. The model is based on a Langevin dynamics simulation. Vortices are

[6] OpenDX is an open-source project based on IBM's Visualization Data Explorer. (`http://www.opendx.org`)

[7] Xmgrace is a scriptable WYSIWYG 2D plotting tool, and a descendant of ACE/gr, also known as Xmgr. (`http://plasma-gate.weizmann.ac.il/Grace`)

[8] PovRay is a Raytracing software to create photo-realistic images of 3D-scenes. (`http://www.povray.org`)

considered as massless point-like particles that repel each other due to their electromagnetic interactions, and are free to move continuously in a two-dimensional area with (periodic) boundary conditions. Vortices experience an underlying pinning potential representing atomic inhomogeneities of the sample, and a Lorentz force representing a transport current. The model describes the physics of a many-body system with competing interactions, and is a good description of a system of pancake vortices (which are not coupled with the other layers) and vortices in thin film superconductors. Such a system is equivalent to the two-dimensional one-component plasma (apart from scaling factors). Using the substrate model (*Fangohr et al.*, 2002) we can also model a three-dimensional layered pancake vortex system in the high anisotropy limit of zero Josephson coupling.

Chapter 3

Efficient methods for handling long-range forces in particle simulations

3.1 Introduction

Considerable effort has been invested in handling long-range forces for particle-particle simulations. The conventional cut-off approach truncates the potential in a single unit cell for separations greater than half the system dimension. In general, it is better to sum the potential over a number of repeats of the unit cell. Infinite summation methods include the Ewald summation (*Ewald*, 1921, *de Leeuw et al.*, 1980, *Allen and Tildesley*, 1989), multipole methods (*Greengard and Rohklin*, 1987), lattice summation methods (*Berman and Greengard*, 1994), the Lekner summation method (*Lekner*, 1989, 1991) and a novel method for logarithmic interactions (*Grønbech-Jensen*, 1996). In this paper we review some of the problems which can occur when the potential is naïvely truncated, which have not previously been widely reported in the literature. We then derive two methods which overcome these problems. The first is suitable for phenomenological studies of systems and smooths the potential within a single unit cell. The second is a new real-space summation method appropriate for potentials governed by Bessel functions. This provides a speed-up factor of at least 20,000 compared to the current method of summing in a series of shells of increasing radius (*Ryu et al.*, 1996).

In section 3.2 we introduce our model system, which is a simulation of the vortex state in a superconductor. We discuss the problems which arise with cutting off the interaction potential in a single unit cell in section 3.3, and give a method of smoothing the potential which overcomes these problems in section 3.4. We detail the implementation of this method in section 3.5. In section 3.6 we consider an infinitely tiled periodic system and derive our new summation method. Section 3.7 describes a simulation of shearing a lattice using our new methods and contrast it with the results obtained when the potential is cut off. Two ways to speed up computations using the suggested methods are described in section 3.8, and we draw our conclusions in section 3.9.

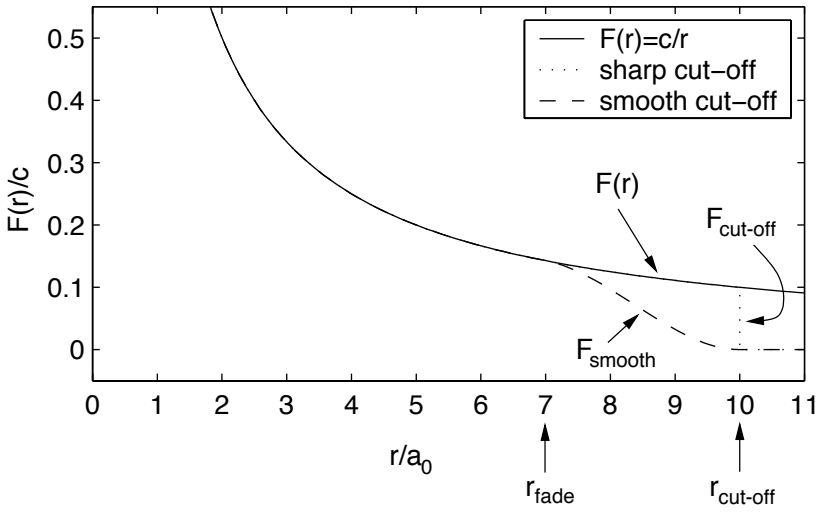

Figure 3.1: A long-range force (solid line), force cut-off at a distance $r_{\mathrm{cut-off}}$ (dotted line), and smoothed force (dashed line). Distances are measured in multiples of the ground-state lattice spacing, a_0.

3.2 Model system

We will consider the long-range forces which arise in the simulation of vortices in high-temperature superconductors (*Clem*, 1998). The interaction potential for vortex lines is (*Tinkham*, 1996):

$$\frac{U(r)}{c} = K_0\left(\frac{r}{\lambda}\right) \tag{3.1}$$

where λ is the penetration depth of the magnetic field, r is the distance between the particles and c is a constant. This may be approximated as

$$\frac{U(r)}{c} = \begin{cases} \sqrt{\frac{\pi\lambda}{2r}}\exp\left(-\frac{r}{\lambda}\right) & : \quad r \to \infty \\ \ln\left(\frac{\lambda}{r}\right) + 0.12 & : \quad r \ll \lambda. \end{cases} \tag{3.2}$$

Since λ in thin films can be several orders of magnitude larger than r (*Ryu et al.*, 1996), the K_0 potential has a very long range (logarithmic) character. It is therefore necessary to either (i) only consider the interaction inside a single unit cell which contains a large number of particles, or (ii) sum the interaction over periodic repeats of the unit cell. Our findings are also of relevance to the simulation of other systems governed by long-range forces such as logarithmically interacting pancake vortices and the two-dimensional one-component electron plasma (*Caillol et al.*, 1982, *de Leeuw and Perram*, 1982) as well as the interaction of electrically charged rods (*Grønbech-Jensen*, 1996). We will show results for Monte Carlo simulations, and for molecular dynamics simulations with a friction term and a random noise term (known as Langevin dynamics, section 2.1). The two-dimensional unit cell geometry can be chosen to be a rectangle, a parallelogram or a hexagon. In all cases periodic boundary conditions are employed.

3.3 Cut-off potential

The standard approach is to cut off the potential to be constant outside a circle of radius smaller or equal to $\min(L_x/2, L_y/2)$, where L_x and L_y are the lengths of the sides of the unit cell. Since the force is the gradient of the potential, it is zero outside the cut-off radius. Considering periodic boundary conditions, we then define the distance between particles, r, to be the minimum image distance (*Allen and Tildesley*, 1989).

In figure 3.1 the real force dependence $F(r)$ (solid line) is compared to that for a simulation system with a simple geometrical cut-off (dotted line). For vortices in superconductors,

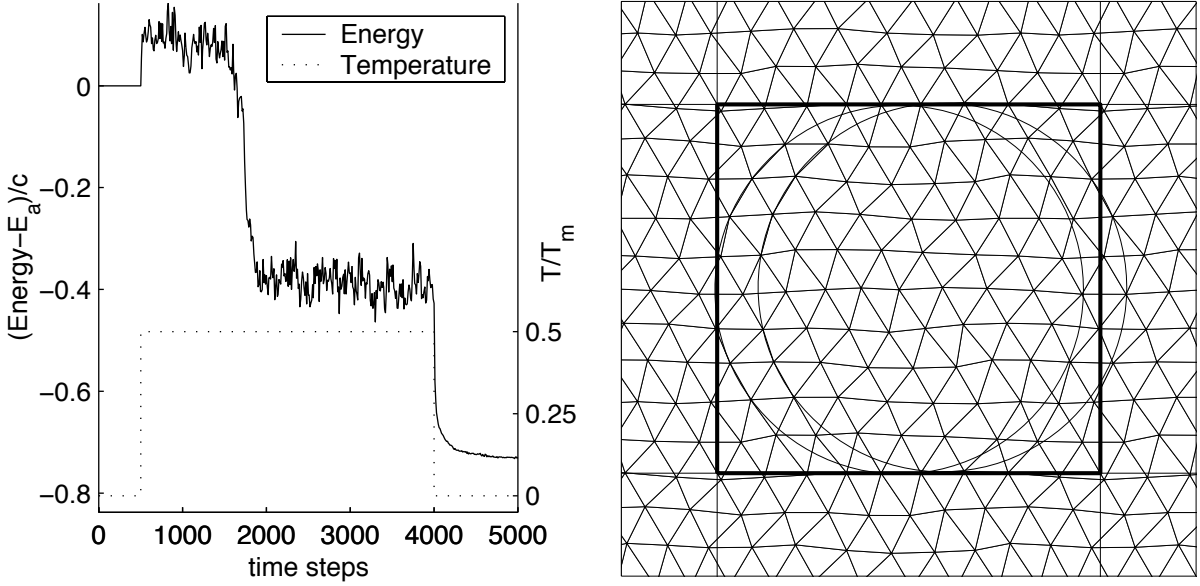

Figure 3.2: Left: Langevin dynamics simulation of 90 particles using a cut-off potential, which start in a hexagonal configuration at 0K (with Abrikosov lattice energy, E_a), are heated to half their melting temperature (T_m) and then returned to 0K. Temperature is introduced via a stochastic noise term (2.4). The system finds a new configuration with energy lower than the energy of the regular lattice. Right: Delaunay triangulation of the final configuration of the particles at time step 5000. Two cut-off circles are shown to demonstrate that particles align along these circles.

Abrikosov (1957) demonstrated theoretically that the lowest energy configuration for an infinite lattice is the hexagonal lattice, or so-called Abrikosov lattice, with an associated Abrikosov lattice energy. However, when using a sharp cut-off in our simulations we find many configurations with energies lower than the Abrikosov lattice energy.

Figure 3.2 shows the results from a Langevin dynamics simulation of a small number of particles in which the temperature in the system is cycled from 0K to half the melting temperature of the vortex solid and is then returned to 0K. The temperature is introduced via a stochastic noise term (2.4). The Delaunay triangulation of the vortex configuration at the end of the simulation is elastically deformed and shown on the right in figure 3.2. Detailed examination of the triangulation shows that the elastic deformations arise due to particles gathering on the boundaries of the cut-off circles. In this position they minimise their contribution to the energy in the system. This gives rise to the "wavy lines" visible in figure 3.2, with a curvature characterised by the cut-off radius. To demonstrate this, we have shown the cut-off circles corresponding to two of the particles. The wavy lines are less evident in larger systems, since their curvature is inversely proportional to the cut-off radius.

If the system is heated above its melting temperature and then annealed slowly, the final equilibrium state (i) has an energy lower than the Abrikosov energy, and (ii) contains topological defects. A topological defect is a particle which does not have six nearest neighbours in the Delaunay triangulation. We have repeated these results for molecular dynamics and Monte Carlo simulations with up to 2000 particles. The result in figure 3.3 for a Monte Carlo simulation of a system annealed from a liquid state exhibits low energy and contains defects. We have verified that our results are independent of the geometry of the unit cell (rectangular, parallelogram, or hexagonal).

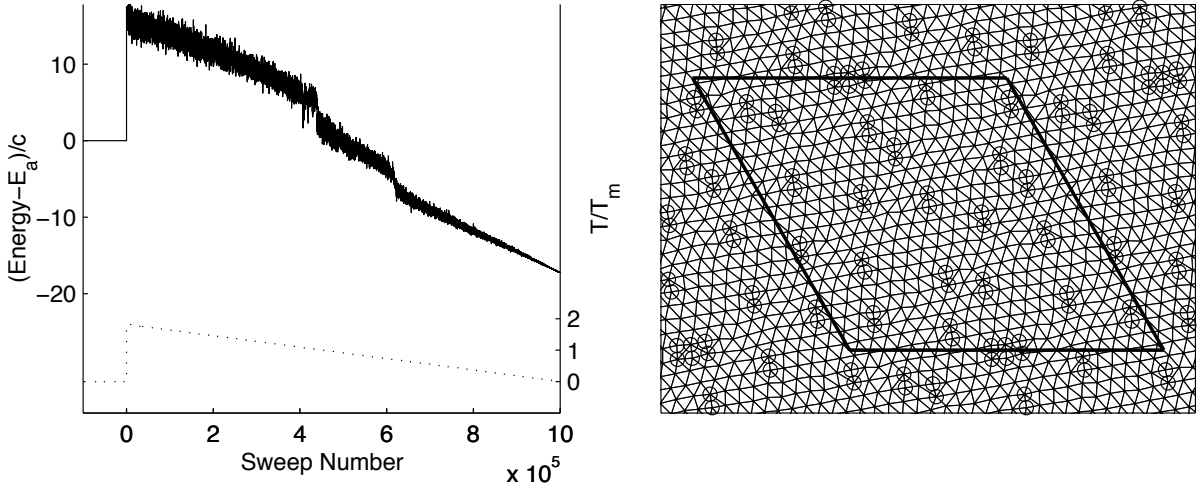

Figure 3.3: Monte Carlo simulation of 432 particles using a conventional cut-off potential. The system starts in a regular hexagonal Abrikosov lattice and is heated above its melting point to approximately $2T_m$ then annealed slowly to zero temperature in steps of $0.01T_m$ each step consisting of 5000 Monte Carlo-sweeps. Left: The energy of the system drops below the Abrikosov lattice energy, E_a. Right: Delaunay triangulation of the final disordered configuration. The topological defects are circled.

These problems are clearly artificial, and are caused by imposing a sharp cut-off on the very long range nature of the interaction. It is possible that these finite size effects disappear for much larger systems, which — depending on the penetration depth, λ — would require systems with several hundred thousand particles before the effects of this problem began to become less significant. Methods to deal with such large systems with the Bessel function interaction potential are currently being developed (*Cox et al.*, 2001), but here we focus on system sizes ≤ 3000 particles which is feasible with today's technologies.

In studies of high temperature superconductors, interest has recently developed in the formation of topologically ordered states which exhibit quasi-long range translational order: the so-called Bragg glass. These states occur when the vortices are weakly pinned and have been investigated both theoretically and experimentally (for example *Giamarchi and Le Doussal*, 1995, *Kokkaliaris et al.*, 1999). Other studies have focused on the structural properties of the dynamics of vortex systems (for example *Higgins and Bhattacharya*, 1996, *Spencer and Jensen*, 1997). In both cases it is important that the ground state for an unpinned system should be a hexagonal lattice without topological defects. Furthermore, for the calculation of numerical phase diagrams as a function of disordering pinning, it is vital that the disorder is not introduced by the model itself.

We therefore propose two methods which avoid the problems described above. The first involves modifying the potential near to the cut-off, and allows qualitative simulation of small systems using only a single unit cell. The second is a fast summation method which allows the infinitely tiled periodic system to be considered and enables quantitative simulations to be performed.

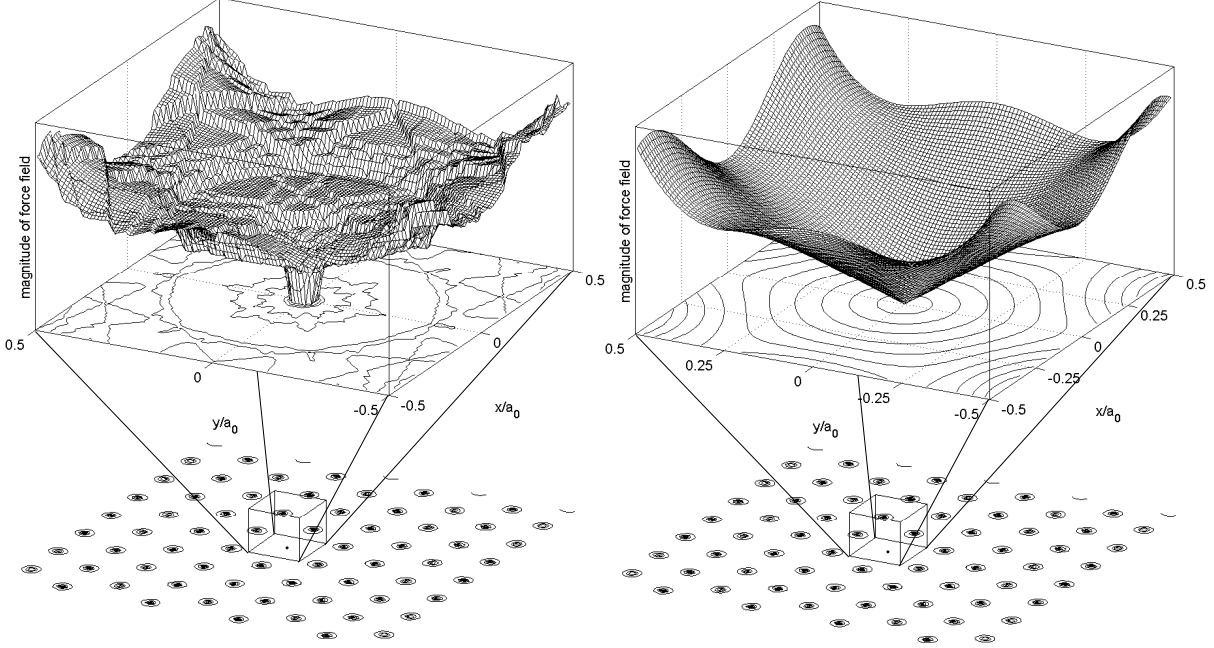

Figure 3.4: The magnitude of the force field that a particle at position (0,0) experiences from a system of 418 particles using (left) the sharp cut-off and (right) the smooth cut-off. Smoothing the potential removes the discontinuities in the force field.

3.4 Smoothed potential

In figure 3.4 (left) we show the force field experienced by a vortex due to its surrounding particles in a hexagonal configuration. The discontinuities are caused by the artificial step in the force function shown in figure 3.1 on page 34. It is natural to introduce a smoothed potential, which reduces the force smoothly to zero over a region from r_{fade} to $r_{\text{cut-off}}$. We impose $\mathcal{C}^1$ continuity of the force at $r = r_{\text{fade}}$ and $r = r_{\text{cut-off}}$, *i.e.* we require the derivative of the force to be continuous at at $r = r_{\text{fade}}$ and $r = r_{\text{cut-off}}$. The smoothed potential is shown in figure 3.1 (dashed line), with the resulting smooth force field in figure 3.4 (right). The smoothing distance $r_{\text{cut-off}} - r_{\text{fade}}$ is a free parameter which should be kept as small as possible to maintain the original force over the largest possible range. Numerical experiments show that three lattices spacings is sufficient. Figure 3.5 shows the results of a Monte Carlo simulation using a similarly smoothed energy. Simulations using this modified potential do not find configurations below the Abrikosov energy and topological defects only occur when the system is annealed very rapidly.

The interpretation is that due to the slow force change at the cut-off (enforced by the derivative being zero) a particle pair separated by a distance of $\approx r_{\text{cut-off}}$ experiences continuous and small changes in force if the relative displacement of the particles is perturbed. This is in contrast to the large discontinuous fluctuations that occur when the sharp cut-off is being used, which can enable the system to discover configurations with energies less than the Abrikosov energy. We have also used interpolating polynomials of higher order and an exponential function in the smoothing region: in all cases the system does not discover energy states below the Abrikosov energy.

It is important to consider whether the modification of the original force with the smooth cut-off affects the system's behaviour. Applying a cut-off to the long-range interaction is a major change of the long-range interaction. However, introducing the smoothing distance and altering the force in the region between r_{fade} and $r_{\text{cut-off}}$ cannot be worse than using a slightly

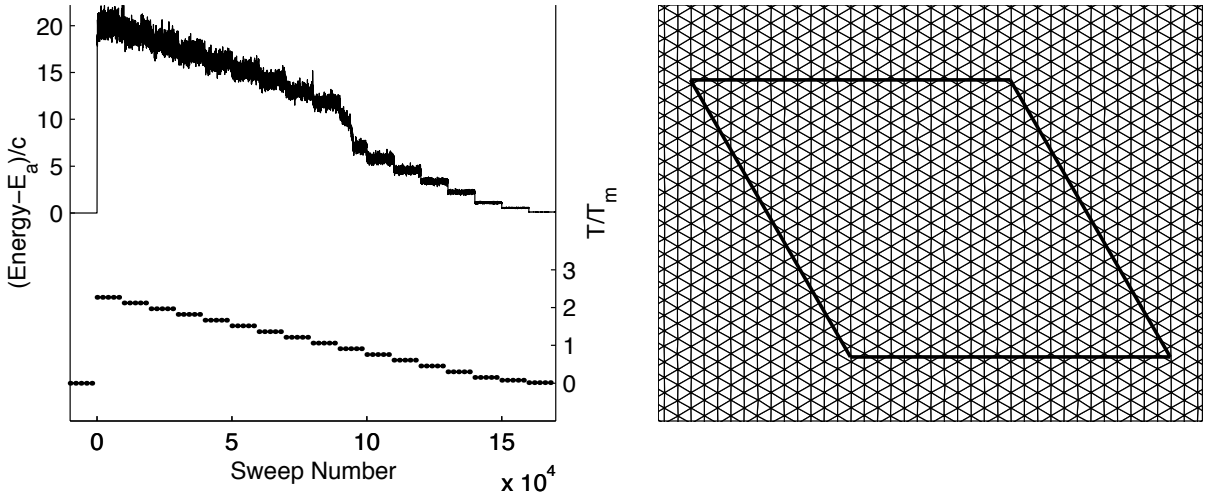

Figure 3.5: Monte Carlo simulation of 432 particles using a potential smoothed over three lattice spacings. Left: The energy of the system never drops below the Abrikosov lattice energy, E_a. Right: Delaunay triangulation of the final configuration shows the system has a hexagonal ground state.

smaller system with $r'_{\mathrm{cut-off}} = r_{\mathrm{fade}}$. The enormous advantage of using a smooth cut-off is that the structural properties of the system can be simulated correctly and that the lowest energy configuration is identical to the known ground state. For studies of the dynamics of vortices, recent results show that the precise details of the long-range particle interaction are not crucial (*Zhu et al.*, 1999), and this is in agreement with our results (see figure 8 in *Fangohr et al.* (2002)) which show no differences between using an infinite lattice summation and using a smooth cut-off. We therefore recommend using the smoothed potential instead of the sharp cut-off.

3.5 Implementation of smooth cut-off

We now describe how to implement a smooth cut-off using a third order polynomial for the force $F(r)\frac{\mathbf{r}}{|\mathbf{r}|} = -\nabla U(r)$, and a fourth order polynomial for the energy $U(r)$.

For short-ranged interactions it is sufficient to use an interaction $\hat{F}(r)$ which is equal to $F(r)$ for $r \leq b$ and zero otherwise:

$$\hat{F}(r) = \begin{cases} F(r) & : \quad r \leq b \\ 0 & : \quad r > b. \end{cases} \tag{3.3}$$

However, to avoid the artificial configurations described above we reduce the long-range force $F(r)$ smoothly to zero near the cut-off distance b as shown in figure 3.6 on the next page. One needs to introduce another distance, a, and a polynomial $p(r)$, such that $a < b$ and that $p(r)$ interpolates between $F(a)$ at a and and zero at b:

$$\hat{F}(r) = \begin{cases} F(r) & : \quad r \leq a \\ p(r) & : \quad a < r \leq b \\ 0 & : \quad r > b. \end{cases} \tag{3.4}$$

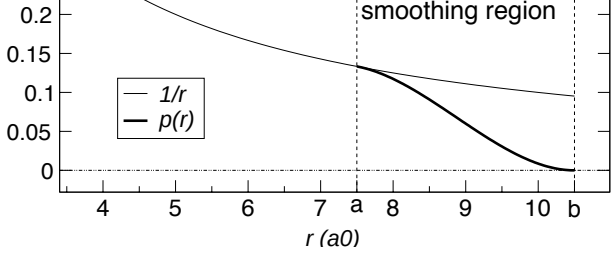

Figure 3.6: Demonstrating the shape of the interpolating polynomial $p(r)$ (thick line) which smoothly reduces the vortex-vortex interaction force $F(r)$ to zero. For clarity we have chosen $F(r) = 1/r$. The interpolation starts at the fading distance $a = 7.5a_0$ and reduces the interaction force to zero at the cut-off distance $b = 10.5a_0$, where a_0 is the average vortex lattice spacing.

It is required that $\hat{F}(r)$ has $\mathcal{C}^1$ continuity at a and b, and its gradient at b is zero:

$$\begin{aligned} F(a) &= p(a), && (3.5)\\ p(b) &= 0, && (3.6)\\ \left.\frac{\mathrm{d}F}{\mathrm{d}r}\right|_{r=a} &= \left.\frac{\mathrm{d}p}{\mathrm{d}r}\right|_{r=a}, && (3.7)\\ \left.\frac{\mathrm{d}p}{\mathrm{d}r}\right|_{r=b} &= 0. && (3.8) \end{aligned}$$

We have used a third order polynomial

$$p(r) = \sum_{i=0}^{3} c_i r^i = c_3 r^3 + c_2 r^2 + c_1 r + c_0 \tag{3.9}$$

and the coefficients c_i are completely determined by equations (3.5) to (3.8). Writing $F'(r)$ for $\frac{\mathrm{d}F}{\mathrm{d}r}(r)$ one finds

$$\begin{pmatrix} c_3 \\ c_2 \\ c_1 \\ c_0 \end{pmatrix} = \frac{1}{(a-b)^3} \begin{pmatrix} F'(a)a - F'(a)b - 2\,F(a) \\ -F'(a)a^2 + 3\,F(a)(a+b) - aF'(a)b + 2\,F'(a)b^2 \\ \left(2\,F'(a)a^2 - aF'(a)b - 6\,F(a)a - F'(a)b^2\right) b \\ -F'(a)b^2a^2 + 3\,F(a)ab^2 + F'(a)ab^3 - b^3F(a) \end{pmatrix}. \tag{3.10}$$

The cut-off distance, b, is determined by geometrical constraints, *i.e.* half the system size, or by the computational resources available. We choose the distance $b - a$ over which the interaction is reduced to zero to be three lattice spacings, so that $a = b - 3a_0$. Figure 3.6 shows a schematic plot of the smooth cut-off and the interpolating polynomial.

To compute the similarly smoothed potential energy of the system, it is required to integrate $-p(x)$ to represent the smoothed interaction potential for $a < r < b$. The integration constant is determined by requiring continuity of the interaction potential at $r = a$.

3.6 Fast infinite summation

An alternative approach to modifying the potential is to sum the potential function over periodic repeats of the unit cell, which provides the best representation of the system given only a finite number of particles. We write the potential (3.1) in the form (*Ryu et al.*, 1996):

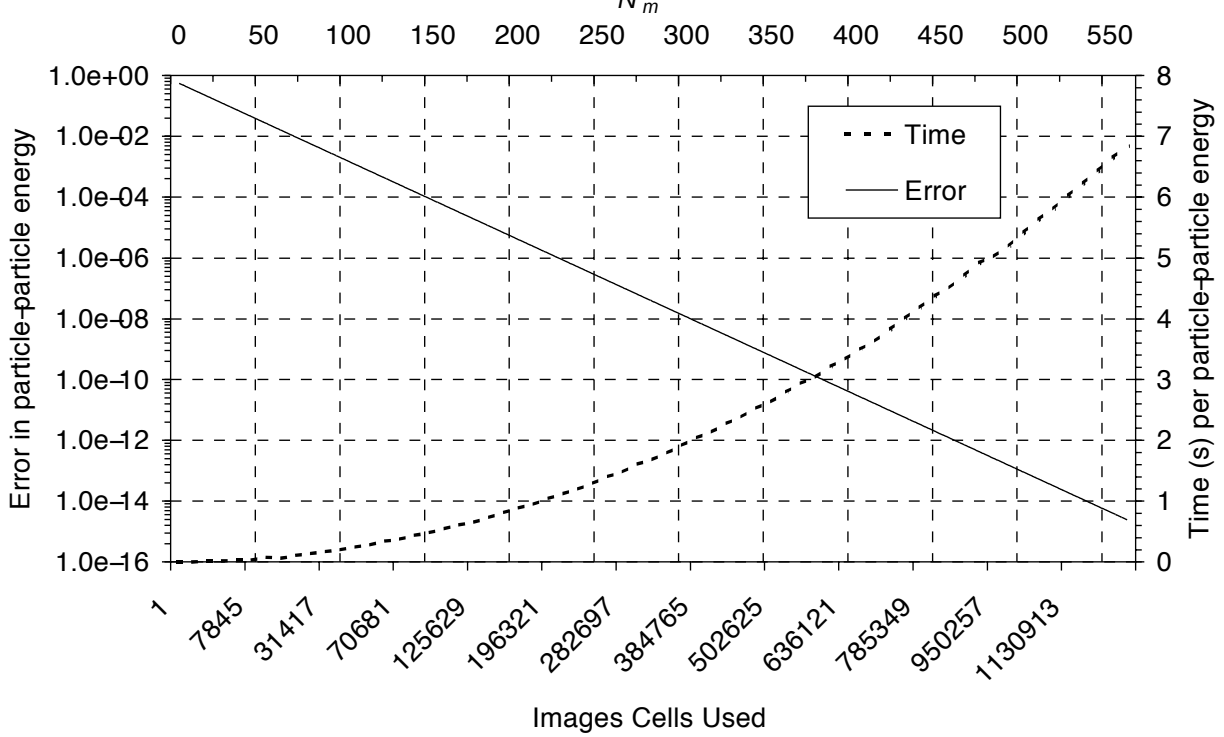

Figure 3.7: Fractional error $(E_\infty - E_n)/E_\infty$ and time taken to compute the energy E_n between two particles separated by a single lattice spacing in an infinitely tiled periodic system when n image cells are used. Here, E_∞ is estimated by allowing the summation to converge to machine accuracy.

$$\frac{U(|\mathbf{r}|)}{c} = K_0^*\left(\frac{|\mathbf{r}|}{\lambda}\right) = \sum_{m_x,m_y} K_0\left(\frac{|\mathbf{r}| + L_x m_x \hat{\mathbf{x}} + L_y m_y \hat{\mathbf{y}}}{\lambda}\right), \tag{3.11}$$

where m_x and m_y are integers and L_x and L_y are the lengths of the edges of the simulation cell. This is truncated such that $m_x^2 + m_y^2 \leq N_m^2$; we sum the potential in shells of increasing radius, N_m, until it has converged.

In order to be able to compare our findings with the results of *Ryu et al.* (1996), we follow their choice of parameter values. We use a value for the penetration depth, λ, at 0K of 7700Å for $Mo_{77}Ge_{23}$. We will return to the temperature dependence of λ later. In figure 3.7, we show the exponentially fast convergence of the energy between two particles in a simulation of 300 vortices in the Abrikosov lattice state, as more image cells are included. We also show the time taken to perform this calculation on a 450 MHz Pentium II using Compaq (Digital) Visual Fortran under Windows NT 4.0. For the particle-particle energy to converge to a relative error better than 1×10^{-8} requires $N_m \sim 300$, which takes approximately $\pi N_m^2 \approx 300,000$ calls to the K_0 function. This ensures that the total system energy is accurate to better than 0.01%.

We now derive a new method to perform this infinite summation. In figure 3.8 we have:

$$\begin{aligned} Z^2 &= (m_x L_x)^2 + (m_y L_y)^2 \\ z^2 &= (x_i - x_j)^2 + (y_i - y_j)^2 \\ \theta &= \tan^{-1}\left(\frac{x_i - x_j}{y_i - y_j}\right) + \frac{\pi}{2} \\ \varphi &= \tan^{-1}\left(\frac{m_y L_y}{m_x L_x}\right). \end{aligned} \tag{3.12}$$

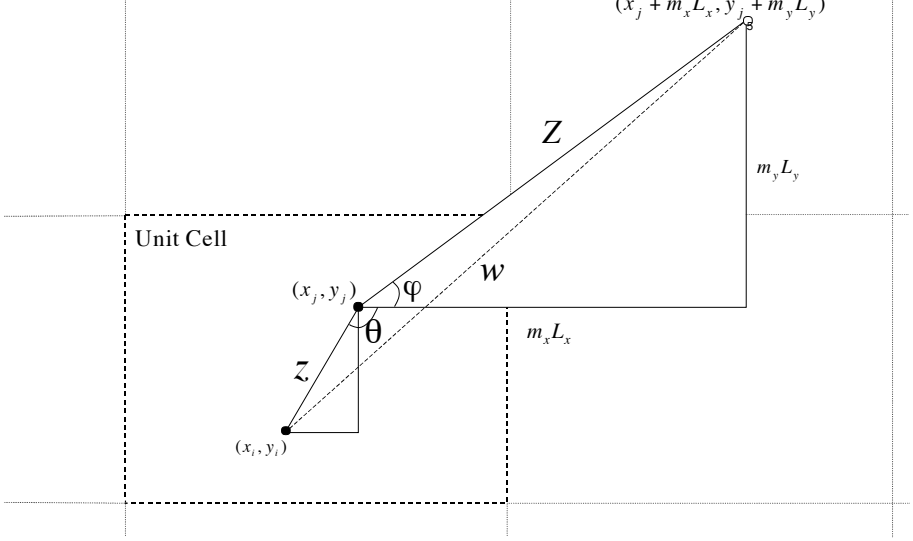

Figure 3.8: Two particles in a unit cell with infinite periodic repeats. Z is the distance from particle i to its own mirror image, z is the distance between i and j, and w is the distance between i and the mirror image of j.

We define

$$\phi = \theta + \varphi$$

which yields

$$w^2 \quad = \quad Z^2 + z^2 - 2zZ\cos(\phi). \tag{3.13}$$

We may use the Gegenbauer addition formulae (*Watson*, 1944) to write

$$K_0\left(\frac{w}{\lambda}\right) = \sum_{k=-\infty}^{\infty} K_k\left(\frac{Z}{\lambda}\right) I_k\left(\frac{z}{\lambda}\right)\cos(k\phi) \tag{3.14}$$

for the energy between a particle i and one of the periodic images of j, where I_k and K_k are modified Bessel functions. This formula requires $z \leq Z$, which is automatically satisfied since z is the minimum image distance between i and j. We can therefore write the total energy (3.11) of two particles i and j summed over all periodic images in the form:

$$K_0^*\left(\frac{|\mathbf{r}|}{\lambda}\right) = K_0^*\left(\frac{w}{\lambda}\right) = K_0\left(\frac{z}{\lambda}\right) + \sum_{\substack{m_x,m_y \\ \text{not } m_x=m_y=0}} \sum_{k=\infty}^{\infty} K_k\left(\frac{Z}{\lambda}\right) I_k\left(\frac{z}{\lambda}\right)\cos(k\phi), \tag{3.15}$$

where the case $m_x = m_y = 0$, for which $z \not< Z$, is the contribution to the energy from the unit cell which must be explicitly included as a separate term. Further re-arrangement and use of (3.13) gives

$$K_0^*\left(\frac{w}{\lambda}\right) = K_0\left(\frac{z}{\lambda}\right) + \sum_{k=-\infty}^{\infty} I_k\left(\frac{z}{\lambda}\right)\left[c_k\cos(k\theta) - s_k\sin(k\theta)\right] \tag{3.16}$$

where

$$\begin{aligned} c_k \quad &= \quad \sum_{\substack{m_x,m_y \\ \text{not } m_x=m_y=0}} K_k\left(\frac{Z}{\lambda}\right)\cos(k\varphi) \\ s_k \quad &= \quad \sum_{\substack{m_x,m_y \\ \text{not } m_x=m_y=0}} K_k\left(\frac{Z}{\lambda}\right)\sin(k\varphi). \end{aligned} \tag{3.17}$$

Equations (3.16) and (3.17) have the remarkable property that the coefficients corresponding to the infinite summation over the periodic repeats of the unit cell can be pre-computed. This reduces the double summation in (3.11) to a single summation. Furthermore, due to the exponential convergence of the Gegenbauer addition formulae, the sum may be truncated at $k_{\text{trunc}} \sim 5 - 20$ terms. A further factor of two in performance can be obtained by using symmetry to convert the summation from $k = -\infty \ldots \infty$ to the range $k = 0 \ldots \infty$.

The form (3.16) closely resembles a Fourier type summation method, yet the whole calculation proceeds in real space in contrast to the Ewald summation method (*Olive and Brandt*, 1998).

The convergence of the energy between two particles in the Abrikosov lattice is identical to the convergence shown in figure 3.7 as we add more terms to the calculation of the coefficients c_k and s_k. We have chosen the case of two nearest neighbours, which yields the slowest convergence of (3.16) since z takes its smallest value.

In a superconductor, λ is a function of the temperature. For our model system ($Mo_{77}Ge_{23}$) $\lambda(T) = \lambda(0)/(1 - T/T_c)^{1/2}$ (*Ryu et al.*, 1996), where $T_c = 5.63$K is the critical temperature at which the material loses its superconducting properties. Hence the coefficients c_k and s_k need to be re-computed at each temperature. As the temperature increases additional image cells need to be included in both (3.11) and the pre-computation (3.17). The crucial difference, however, between (3.11) and (3.16) is that the time taken to evaluate the energy using (3.16) remains virtually constant once the coefficients are available, whereas the na"ıve summation requires considerable numbers of additional image cells to converge to the solution. In figure 3.9 we show the speedup of our method when computing the energy between two particles at a fixed accuracy of 1×10^{-5} (relative to the energy computed to machine accuracy by either method). In all cases the resulting energies are shown to be identical to the stated accuracy. At 0K and using 5 terms in the truncation of (3.16), we have a speedup of 20,000 over the naïve summation method. This rises to 400,000 for temperatures approaching T_c. If the particle energy is required to be accurate to 1×10^{-8}, then, using 30 coefficients, the speedups are between 50,000 (T = 0K) and 1,000,000 ($T \approx T_c$).

Since the coefficients c_k and s_k depend on λ (and hence temperature); the method may appear to be costly if the temperature is changed at every Langevin dynamics or Monte Carlo step. We now discuss several ways to overcome this. Firstly, it is possible to perform Monte Carlo simulations at a small number of temperatures and use the data from these to obtain information about the behaviour of the system as a continuous function of temperature (*Ferrenberg and Swendsen*, 1988, 1989). Thus improving the sophistication of the analysis of the results can reduce the number coefficients c_k and s_k which need to be pre-calculated. Secondly it is possible to compute the c_k and s_k at a small set of temperatures and use interpolation to derive their values at other temperatures. Finally, since only $\sim 5 - 20$ coefficients are needed, it is straightforward to compute once and store on disk the values of c_k and s_k for each temperature to be explored. These values will be re-used a large number of times in a typical set of numerical simulations.

We implement (3.16) using a recurrence relation (*Press et al.*, 1992) for the trigonometric terms and a vendor-optimised vector Bessel function. Goertzel's algorithm (*Goertzel*, 1958) could be employed for additional efficiency, though the improvement is likely to be marginal. The remarkable speedup obtained is due to the fixed work equivalent to roughly five calls to a Bessel function routine required for (3.16), compared to $\sim 100,000$ calls required for (3.11) (at 0K). The five calls are: two to initialise the Bessel recurrence, one to evaluate the contribution from the unit cell, and the equivalent of roughly a further two for the remaining trigonometric terms.

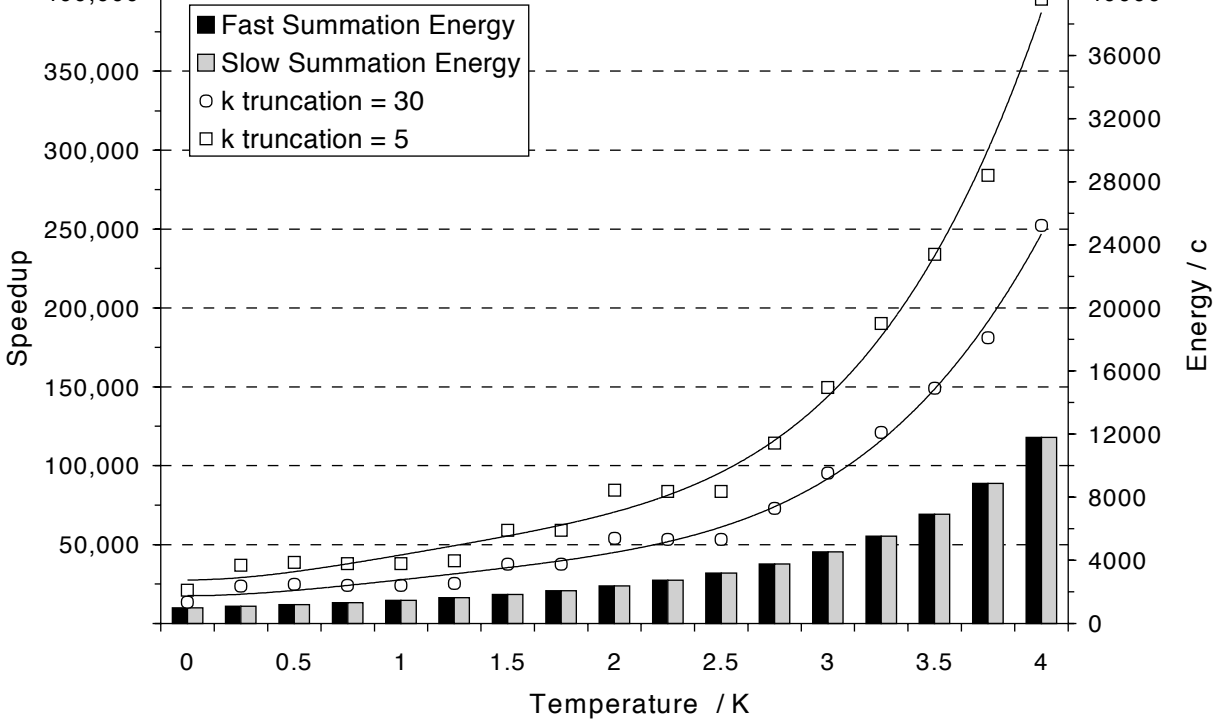

Figure 3.9: Speedup of fast infinite summation method over naïve implementation when the relative error in the energy between each pair of particles is fixed to be 1×10^{-5}: both methods yield identical results.

Our infinite summation is correspondingly five times slower than using the smoothed potential in a single unit cell, which requires evaluation of a single Bessel function or a polynomial. This is confirmed by experiments. For simulations using the fast infinite lattice summation, results are similar to those of figure 3.5. The infinite lattice summation method is suitable for quantitative studies of superconductors.

3.7 Results

In the previous sections we have demonstrated that the phenomenological potential and the infinitely summed potential ensure that the Abrikosov lattice is the minimum energy configuration for our system. We now show that the incorrect handling of the long-range potential seriously affects the elastic properties of a lattice.

We have considered a simulation of shearing of a hexagonal lattice, which is a simplified version of the simulations required to perform current-voltage characterisations. Inset (a) in figure 3.10 shows a Delaunay triangulation for half the simulation cell demonstrating the experimental set-up: a shearing force is applied to the central row of particles marked by black points, and the particles marked by open circles are not allowed to move in the x-direction. The main diagram shows the resulting change in energy as a response to the shearing force. The upper part of the figure shows data for the smooth cut-off, and the lower part shows the results for the sharp cut-off. The smooth cut-off and the infinite lattice summation produce the expected behaviour: with increasing shear stress the energy increases. The slope of the energy-change as a function of the displacement characterises the shear elastic modulus of the crystal. Inset (b1) shows a triangulation of a system which has been slightly tilted by the applied force. In contrast, employing the sharp cut-off, the energy decreases for applied shear stress, *i.e.* the material

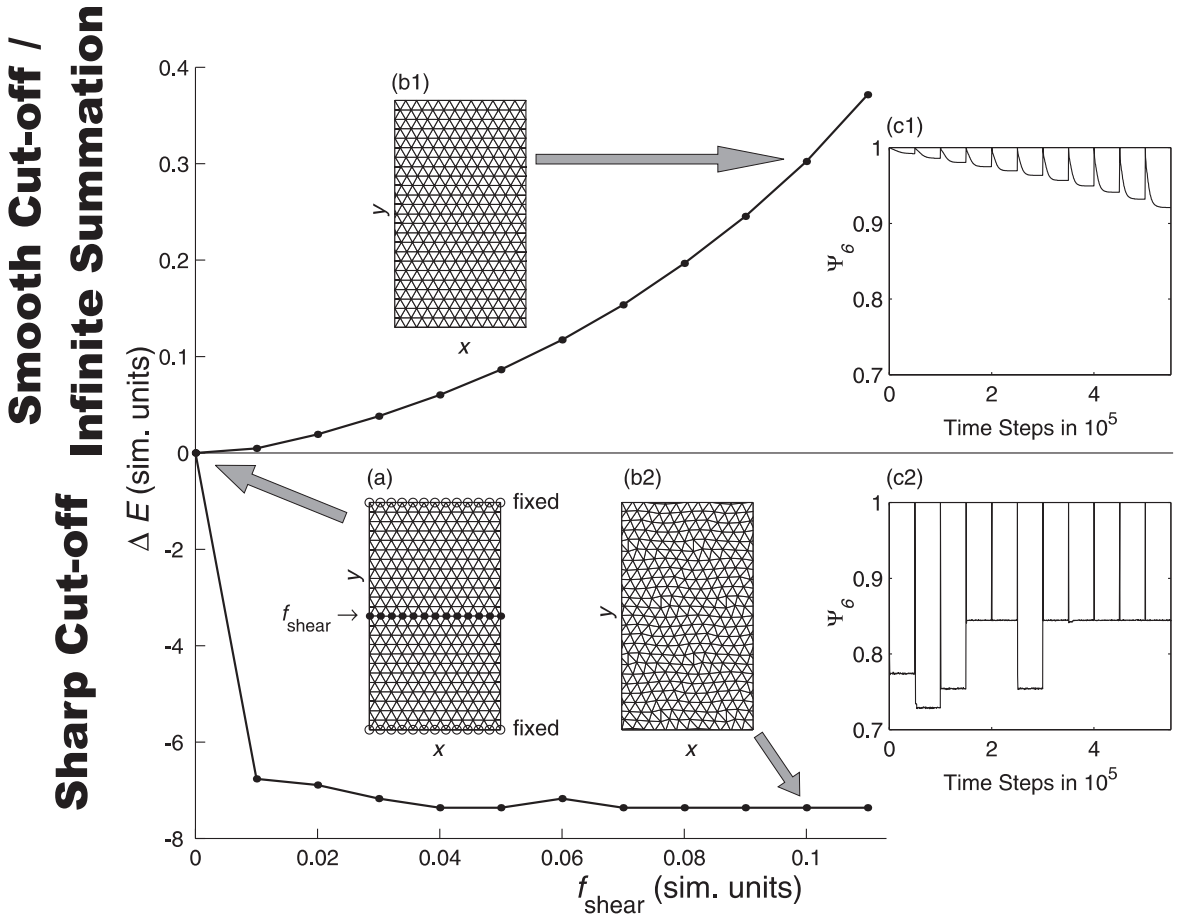

Figure 3.10: Change in energy, ΔE, (in simulation units) as a function of a shearing force, f_{shear}, (in simulation units) for the smooth and the sharp cut-off. For the infinite lattice summation we obtain qualitatively similar results. Insets (a), (b1) and (b2) show different snap shots of vortex configurations. Insets (c1) and (c2) show the local hexagonal order, Ψ_6, as the experiment progresses (see text for details).

appears to collapse after applying a shearing force! We show the triangulation of the particle configuration after shearing in inset b2.

Insets (c1) and (c2) show the time evolution of the local hexatic order (section 2.9.7),

$$\Psi_6 = \frac{1}{n_{\text{bond}}} \left| \sum_k \exp(i6\theta_k) \right|, \tag{3.18}$$

where the sum runs over all bond angles θ_k in the Delaunay triangulation. Every 50,000 time steps the system starts as a hexagonal lattice ($\Psi_6 = 1$) and a new shearing force is applied for the next 50,000 time steps.

In (c1), which shows results computed using the smoothed potential, Ψ_6 decreases continuously until a static state is reached, reflecting the shearing of the system. The energy data in the main plot are taken from these static states. In (c2) (sharp cut-off) Ψ_6 drops suddenly to a much smaller value, representing the sudden change to configurations similar to those shown in (b2). Thus, using a sharp cut-off, the mechanical properties of the lattice are severely affected by the incorrect handling of the long-range potential: this would seriously affect numerical simulations aimed at studying elastic properties of the vortex state in superconductors. The smooth cut-off

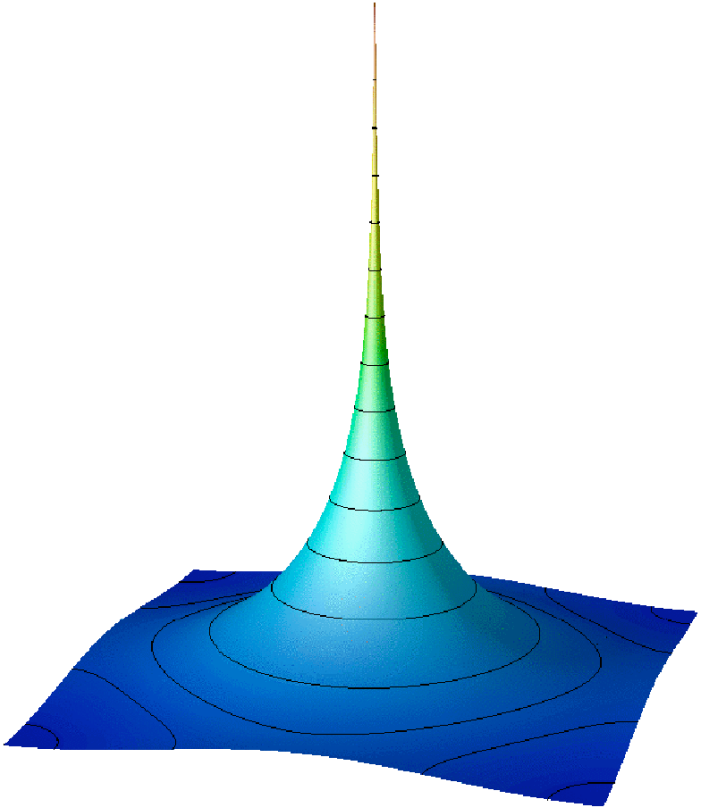

Figure 3.11: Infinite lattice interaction potential $U(\mathbf{r})$ as a function of particle-pair displacement vector $\mathbf{r} \in \mathcal{S}$ within the simulation cell $\mathcal{S}$. For $\mathbf{r} \to \mathbf{0}$ the particles approach each other and feel a strong repulsive force, which is reflected in the divergence in the centre (at $\mathbf{r} = 0$). Note that the isolines are not equally spaced, which reveals the periodicity of the system close to the corners.

and the infinite lattice summation produce the correct physical behaviour and can be used in more complex numerical simulations for phenomenological (smoothed potential) or quantitative (infinite summation) studies of the vortex state.

In comparative studies, we have found that it makes no difference whether the infinite lattice summation or the smooth cut-off is used for our simulations (for example, figure 8 in *Fangohr et al.* (2002) shows the agreement of data computed with either method).

3.8 Efficiency improvements

We describe how to further speed up particle simulations when using an infinite lattice summation (section 3.8.1) and a cut-off (section 3.8.2).

3.8.1 Look-up table for infinite lattice summation

For every interacting particle-pair $(\mathbf{r}_i,\ \mathbf{r}_j)$ with $i \neq j$, the infinite lattice summation can be seen as computing the interaction between two lattices that are displaced relative to each other by the displacement vector $\mathbf{r} = \mathbf{r}_i - \mathbf{r}_j$, where the unit cell for the displaced lattices is the simulation cell. The displacement vector $\mathbf{r}$ will always be located within the simulation cell $\mathcal{S} = [-L_x/2, L_x/2] \times [-L_y/2, L_y/2] \subset \mathbb{R}^2$.

We can use this property, and pre-compute a look-up table for (3.16) for all $\mathbf{r} \in \mathcal{S}$. We know that the interaction potential $U(\mathbf{r})$ diverges[1] at $\mathbf{r} = \mathbf{0}$, but varies slowly and smoothly for all other $\mathbf{r} \in \mathcal{S}$. Due to the strong repulsion, particles will not come close to each other so that it is not necessary to pay special attention to the divergence.

[1] We do not take into account here the attraction that real vortices experience when their cores start to overlap.

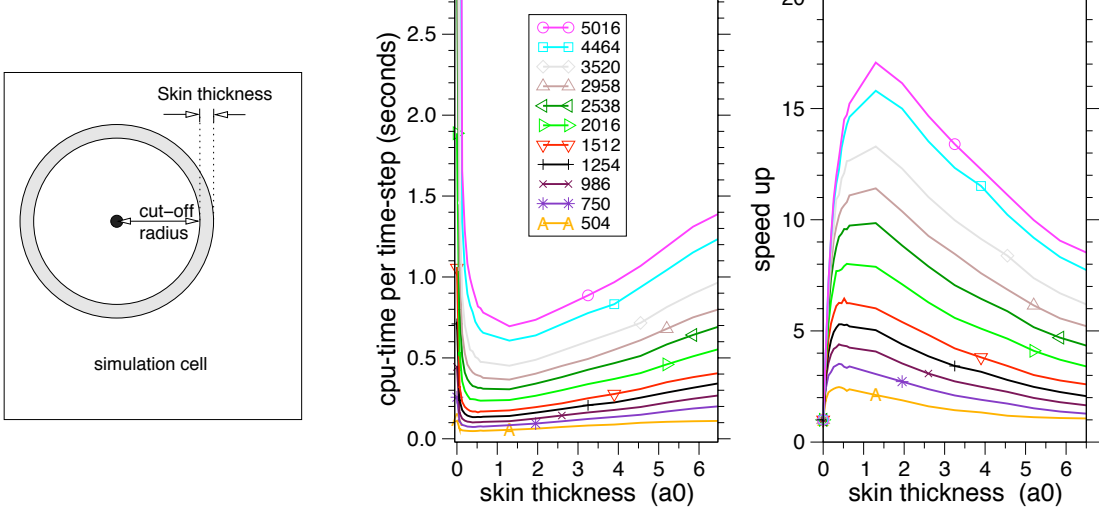

Figure 3.12: *Left:* For the neighbour look-up, we keep for each particle a list containing all other particles inside the cut-off circle and inside the skin-layer (shaded in gray). *Middle:* Performance results for a cut-off at $6.5a_0$, where a_0 is the average particle spacing. The thickness of the skin-layer has been varied from 0 to $6.5a_0$. Each line is for another number of particles, as indicated in the legend. *Right:* Speed-up relative to using no neighbour list. The optimum skin thickness varies with the system size, and shifts from $\approx 0.4a_0$ for 504 particles to $\approx 1.5a_0$ for 5016 particles.

Figure 3.11 shows the infinite lattice interaction potential $U(\mathbf{r})$ with $\mathbf{r} \in \mathcal{S}$ for a logarithmic particle interaction as described by *Grønbech-Jensen* (1996), which shows qualitatively the same features as the infinite-lattice interaction potential for K_0, only with the central divergence decaying slower with increasing $\mathbf{r}$. The figure demonstrates the regularity of this function for $\mathbf{r} \neq \mathbf{0}$.

Such a smooth function (apart from $\mathbf{r} = \mathbf{0}$) can easily be interpolated by a two-dimensional look-up table using bi-linear or bi-cubic interpolation for intermediate positions. In the beginning of a simulation, we have a small overhead to compute the look-up table which can be done within a couple of minutes (for 600 particles, 2000 table-entries per area occupied by one particle, on a 700 MHz PIII). However, subsequently we profit strongly from the look-up table: it is (i) about as fast as the smooth cut-off, and (ii) we can pre-compute the table with a high accuracy without slowing down the subsequent main computation.

3.8.2 Neighbour list for smooth cut-off

Having confirmed that using a (smooth) cut-off is an appropriate method to study a system, one can consider to cut off the interaction not at the largest possible value (*i.e.* half the simulation cell size), but for example at a distance of 10 lattice spacings. It is advisable to perform finite size scaling to ensure that this does indeed not affect the system. Having done so, we can keep a neighbour list for every particle which keeps all particles within the cut-off range and particles just outside the cutoff range. This method is known as a Neighbour-list or Verlet-list (*Verlet*, 1967).

The left plot in figure 3.12 demonstrates the concept of the skin layer. In the very first time-step, we create the neighbour lists. Subsequently, in every time step n, we find the maximum

displacement Δr^n

$$\Delta r^n = \max_i |\dot{\mathbf{r}}_i^n \Delta t| \tag{3.19}$$

where $\dot{\mathbf{r}}_i^n$ is the velocity of particle i in time-step n. We recompute the neighbour list when

$$\sum_n \Delta r^n \geq d_{\text{skin}} \tag{3.20}$$

where d_{skin} is the thickness of the skin-layer. To compute the interaction of a particle with all others, we now only consider particles within the cut-off circle and within the skin-layer, and these can be looked up quickly from the neighbour list.

Apart from the re-computation of the neighbour list, the time complexity scales linear with the number of particles for a given cut-off and a fixed thin thickness. The performance data shown in figure 3.12 help us to chose the optimum skin-thickness: if the skin-layer is too thick, then many unnecessary interaction computations are attempted with the particles in the skin-layer. On the other hand, if the skin-layer is too thin, then the neighbour list needs to be updated very frequently, which is quite expensive. The data show that even for small systems there is a performance gain using the neighbour look-up, and for large systems it can be substantial. Even if the cut-off is chosen to be half the system size, there is still a performance increase by using a thin skin-layer in comparison to not using a neighbour list.

3.9 Conclusions

For particle-particle simulations using long-range interactions subject to periodic boundary conditions, a sharp cut-off for the interaction energy (or force) can yield misleading results. We have considered the case of superconductors, in which the potential is governed by a Bessel function. Monte Carlo and molecular dynamics simulations are often used to study phase diagrams numerically and it is vital that the phase behaviour of the system is not affected by the model itself. We find that using a sharp cut-off the system can find irregular lattice configurations with an energy below the theoretical ground state of a regular hexagonal lattice. Therefore, the (dynamical) phase diagram of the system under investigation can be dramatically affected by incorrect handling of the long-range potential.

We have presented two methods which overcome these problems. The first is suitable for phenomenological studies of systems and uses a smoothed potential, but still truncates the interaction over a single unit cell. Annealing a system governed by this modified potential yields a perfect hexagonal lattice which is the global energy minimum. This is the least computationally expensive option and is applicable to any potential. The second method sums the interaction over the infinitely tiled unit cell and is suitable for quantitative system studies. Previous methods for performing this, add the tiled images in a series of shells of increasing radius. We have shown that with the pre-computation of a set of Fourier type coefficients, the whole infinite summation can be computed using a summation which converges exponentially fast and results in a speed-up of between 20,000 and 1,000,000 over the naïve summation, depending on the range of the interaction and the desired accuracy. The derivation of the summation proceeds in real space, and the results converge exactly to those obtained from other summation methods. This is roughly five times as slow as using the smoothed potential, but is the most accurate method for systems of finite size. Both methods can be made faster by using looking look-up tables for the interaction (infinite lattice summation) and for neighbours (smooth cut-off). The suggested methods have been used in *Fangohr et al.* (2001b,a, 2002) and in a number of other works (*Price et al.*, 2000, *Molinari et al.*, 2001, *Fruchter*, 2002b,a, *Grigorenko et al.*, 2002).

To do

- combine this document with the userguide for vdsim

Bibliography

Abrikosov AA. On the magnetic properties of superconductors of the second group. *Soviet Physics–JETP*, **5**, 1174–1182 (1957).

Allen MP and Tildesley DJ. *Computer Simulations of Liquids*. Clarendon Press, Oxford (1989).

Aranson I and Vinokur V. Surface instabilities and vortex transport in current-carrying superconductors. *Physical Review B*, **57**, 3073–3083 (1998).

Aranson IS, Scheidl S and Vinokur VM. Non-equilibrium dislocation dynamics and instability of driven vortex lattices in two dimensions. *Physical Review B*, **58**, 14541–14547 (1998).

Artemenko SN and Kruglov AN. Structure of 2d vortex in a layered high-T_c superconductor. *Phys. Lett. A*, **143**, 485–488 (1990).

Barber CB, Dobkin DP and Huhdanpaa H. The quickhull algorithm for convex hulls. *ACM Transactions on Mathematical Software*, **22**, 469–483 (1996).

Bardeen J, Cooper LN and Schrieffer JR. Theory of superconductivity. *Phys. Rev.*, **108**, 1175–1204 (1957).

Bardeen J and Stephen MJ. Theory of the motion of vortices in superconductors. *Phys. Rev.*, **140**, A1197–A1207 (1965).

Bednorz JG and Müller KA. Possible high T_c superconductivity in the Ba-La-Cu-O system. *Z. Physik B*, **64**, 189 (1986).

Berman CL and Greengard L. A renormalization method for the evaluation of lattice sums. *J. Math. Phys.*, **35** (1994).

Blatter G, Feigel'man MV, Geshkenbein VB, Larkin AI and Vinokur V. Vortices in high-temperature superconductors. *Reviews of Modern Physics*, **66**, 1125–1388 (1994).

Bou-Diab M, Dodgson MJW and Blatter G. Vortex collisions: Crossing or recombination. *Physical Review Letters*, **86**, 5132–5135 (2001).

Brandt EH. The flux-line lattice in superconductors. *Reports on Progress in Physics*, **58**, 1465–1594 (1995).

Brass A, Jensen HJ and Berlinsky A. Models of flux pinning in the quasi-static limit. *Physical Review B*, **39**, 102–116 (1989).

Braun D, Crabtree GW, Kaper HG, Koshelev AE, Leaf G, Levine DM and Vinokur VM. Structure of a moving vortex lattice. *Physical Review Letters*, **76**, 831 (1996).

Buckel W. *Supraleitung. Grundlagen und Anwendungen*. VCH Verlagsgesellschaft, Weinheim, Germany, 5th edition (1993).

Bulaevskii LN, Ledvij M and Kogan VG. Distorted vortex in josephson-coupled layered superconductors. *Physical Review B*, **46**, 11807–11812 (1992).

Buzdin A and Feinberg D. *J. Phys. (France)*, **51**, 1971 (1990).

Caillol JM, Levesque D, Weis JJ and Hansen JP. A Monte Carlo study of the classical two-dimensional one-component plasma. *Journal of Statistical Physics*, **28**(2), 325–349 (1982).

Chaikin PM and Lubensky TC. *Principles of condensed matter physics*. Cambridge University Press, Cambridge (1995).

Choquard P. Cooperative phenomena below melting of the one-component two-dimensional plasma. *Physical Review Letters*, **50**, 2086–2089 (1983).

Clem JR. Two-dimensional vortices in a stack of thin superconducting films: A model for high-temperature superconducting multilayers. *Physical Review B*, **43**, 7837–7846 (1991).

Clem JR. Anisotropy and two-dimensional behaviour in the high-temperature superconductors. *Supercond. Sci. Technol.*, **11**, 909–914 (1998).

Cox SJ, Daniell GJ, Fangohr H and Robinson AM. An $\mathcal{O}(N)$ multipole algorithm for the 2d Helmholtz equation (2001). Submitted.

de Berg M, van Kreveld M, Overmars M and Schwarzkopf O. *Computational Geometry*. Springer Verlag, Berlin (1997).

de Leeuw SW and Perram JW. Statistical mechanis of two-dimensional coulomb systems. *Physica*, **113A**, 546–558 (1982).

de Leeuw SW, Perram JW and Smith ER. Simulation of electrostatic systems in periodic boundary conditions. I. Lattice sums and dielectric constants. *Proceedings of the Royal Society of London*, **373**, 27–56 (1980).

Domínguez D. Dynamic transition in vortex flow in strongly disordered Josephson junction arrays and superconducting thin films. *Physical Review Letters*, **82**, 181–184 (1999).

Ewald PP. Die Berechnung optischer und elektrostatischer Gitterpotentiale. *Annalen der Physik*, **64**, 253–287 (1921).

Fangohr H, Cox SJ and de Groot PAJ. Vortex dynamics in two-dimensional systems at high driving forces. *Physical Review B*, **64**, 064505 (2001a).

Fangohr H, de Groot PAJ and Cox SJ. Critical transverse forces in weakly pinned driven vortex systems. *Physical Review B*, **63**, 064501 (2001b).

Fangohr H, Koshelev AE and Dodgson MJW. Vortex matter in layered superconductors without josephson coupling: numerical simulations within mean field approach. *cond-mat/0210580* (2002). Submitted to Phys. Rev. B.

Fangohr H, Price A, Cox S, de Groot PAJ, Daniell GJ and Thomas KS. Efficient methods for handling long-range forces in particle-particle simulations. *J. Comput. Phys.*, **162**, 372–384 (2000).

Feigel'man MV, Geshkenbein VB and Larkin AI. Pinning and creep in layered superconductors. *Physica C*, **167**, 177–187 (1990).

Ferrenberg AM and Swendsen RH. New Monte Carlo technique for studying phase transitions. *Physical Review Letters*, **61**, 2635–2638 (1988).

Ferrenberg AM and Swendsen RH. Optimized Monte Carlo data analysis. *Physical Review Letters*, **63**, 1195–1198 (1989).

Frigo M and Johnson SG. FFTW : an adaptive software architecture for the FFT. In *1998 ICASSP conference proceedings*, volume 3, pages 1381–1384 (1998).

Fruchter L. Metastable states of a driven flux lattice in a superconductor with strong pins. *Physica C*, **370**, 157–162 (2002a).

Fruchter L. Transition to plastic motion as a critical phenomenon and anomalous interface layer of a 2d driven vortex lattice. *Eur. Phys. J. B*, **25**, 313–317 (2002b).

Geometry Centre. Center for the computation and visualization of geometric structures. www.geom.umn.edu (1999).

Giamarchi T and Le Doussal P. Elastic theory of flux lattices in the presence of weak disorder. *Physical Review B*, **52**, 1242–1270 (1995).

Ginzburg VL and Landau LD. *Zh. Eksperim. Teor. Fiz.*, **20**, 1064 (1950).

Goertzel G. An algorithm for the evaluation of finite trigonometric series. *American mathematical monthly*, **34** (1958).

Gordeev S (2000). Private communication.

Gorkov LP. *Sov. Phys.—JETP*, **9**, 1364 (1959).

Greengard L and Rohklin V. A fast algorithm for particle simulations. *J. Comp. Phys.*, **73**, 325 (1987).

Grigorenko AN, Bending SJ, Fangohr H, Bael MJV, Bekaert J, Lange M and Moshchalkov VV. Symmetry locking and domain formation in commensurate structures (2002). In preparation for submission.

Grønbech-Jensen N. Summation of logarithmic interactions in periodic media. *Intern. J. Mod. Phys. C*, **7**, 873–881 (1996).

Grønbech-Jensen N, Bishop AR and Domínguez D. Metastable filamentary vortex flow in thin film superconductors. *Physical Review Letters*, **76**, 2985–2988 (1996).

Gropp WD, Kaper HG, Leaf GK, Levine DM, Palumbo M and Vinokur VM. Numerical simulation of vortex dynamics in type II superconductors. *J. Comp. Phys.*, **123**, 254–266 (1996).

Groth J, Reichhardt C, Olson CJ, Field SB and Nori F. Vortex plastic motions in twinned superconductors. *Physical Review Letters*, **77**, 3625–3628 (1996).

Haile JM. *Molecular Dynamics Simulation, Elementary Methods*. John Wiley & Sons, professional paperback edition (1997).

Higgins MJ and Bhattacharya S. Varieties of dynamics in a disordered flux-line lattice. *Physica C*, **257**, 232–254 (1996).

Kamerlingh Onnes H. *Leiden Comm.*, **120b** (1911).

Kittel C. *Introduction to Solid State Physics*. John Wiley & sons, 7th edition (1996).

Kohandel M and Kardar M. Melting of flux lines in an alternating parallel current. *Physical Review B*, **59**, 9637–9641 (1999).

Kokkaliaris S, de Groot PAJ, Gordeev SN and Zhukov AA. Onset of plasticity and hardening of the hysteretic response in the vortex system of $YBa_2Cu_3O_{7-\delta}$. *Physical Review Letters*, **82**, 5116–5119 (1999).

Koshelev AE and Vinokur VM. Dynamic melting of the vortex lattice. *Physical Review Letters*, **73**, 3580–3583 (1994).

Kubo R, Toda M and Hashitsume N. *Statistical Physics II, Nonequilibrium Statistical Mechanics*. Springer-Verlag (1985).

Kunchur MN, Christen DK and Phillips JM. Observation of free flux flow and high dissipation levels in $YBa_2Cu_3O_{7-\delta}$ epitaxial films. *Physical Review Letters*, **70**, 998–1001 (1993).

Lawrence WE and Doniach S. In E Kanda, editor, *Proceedings of the Twelfth International Conference on Low Temperature Physics*, page 361. Academic Press of Japan, Kyoto (1971).

Lekner J. Summation of dipolar fields in simulated liquid vapor interfaces. *Physica A*, **157**, 826–838 (1989).

Lekner J. Summation of Coulomb fields in computer-simulated disordered-systems. *Physica A*, **176**, 485–498 (1991).

Lenk R and Gellert W. *Fachlexikon abc Physik*, volume 1. Harri Deutsch, Frankfurt/M., Leipzig, 2nd edition (1989).

Li YH and Teitel S. Phase transitions and vortex-line entanglement in a model high-temperature superconductor. *Physical Review B*, **49**, 4136–4144 (1994).

London F and London H. The electromagnetic equations of the supraconductor. *Proceedings of the Royal Society of London*, **A149**, 71–88 (1935).

Metropolis NA, Rosenbluth AW, Rosenbluth MN, Teller AH and Teller E. Equation of state calculations by fast computing machins. *J. Chem. Phys.*, **21**, 1087–1092 (1953).

Molinari M, Fangohr H, Generowicz J and Cox SJ. Finite element optimizations for efficient non-linear electrical tomography reconstruction. In *Proceedings of the 2nd World Congress on Industrial Process Tomography*, pages 406–417 (2001).

Moon K, Scalettar RT and Zimányi GT. Dynamical phases of driven vortex systems. *Physical Review Letters*, **77**, 2778–2781 (1996).

Nagamatsu J, Nakagawa N, Muranaka T, Zenitani Y and Akimitsu J. Superconductivity at 39 K in magnesium diboride. *Nature*, **410**, 63 (2001).

Nguyen AK and Sudbø A. Topological phase fluctuations, amplitude fluctuations, and criticality in extreme type-II superconductors. *Physical Review B*, **60**, 15307–15331 (1999).

Nordborg H and Blatter G. Vortices and 2d bosons: A path-integral Monte Carlo study. *Physical Review Letters*, **79**, 1925–1928 (1997).

Olive E and Brandt EH. Point defects in the flux-line lattice of superconductors. *Physical Review B*, **57**, 13861–13871 (1998).

Olson CJ and Reichhardt C. Transverse depinning in strongly driven vortex lattices with disorder. *Physical Review B*, **61**, R3811–R3814 (2000).

Olson CJ, Reichhardt C and Nori F. Fractal networks, braiding channels, and voltage noise in intermittently flowing rivers of quantized magnetic flux. *Physical Review Letters*, **80**, 2197–2200 (1998a).

Olson CJ, Reichhardt C and Nori F. Nonequilibrium dynamic phase diagram for vortex lattices. *Physical Review Letters*, **81**, 3757–3760 (1998b).

Pearl J. *Appl. Phys. Lett.*, **5**, 65 (1964).

Pippard AB. An experimental and theoretical study of the relation between magnetic field and current in a superconductor. *Proceedings of the Royal Society of London*, **A216**, 547–568 (1953).

Press WH, Teukolsky SA, Vetterling WT and Fannery BP. *Numerical Recipes in Fortran*. Cambridge University Press, 2nd edition (1992).

Price AR, Fangohr H, Cox SJ and de Groot PA. Monte Carlo simulation of layered high temperature superconductors. *Physica C*, **341-348**, 1303–1304 (2000).

Rademacher M. Single molecules feel the force. *Physics World*, pages 33–37, September (1999).

Rapaport DC. *The Art of Molecular Dynamics Simulation*. Cambridge University Press, Cambridge, Great Britain, 1st edition (1995).

Ryu S, Hellerqvist M, Doniach S, Kapitulnik A and Stroud D. Dynamical phase transition in a driven disordered vortex lattice. *Physical Review Letters*, **77**, 5114–5118 (1996).

Ryu S and Stroud D. First-order melting and dynamics of flux lines in a model for $YBa_2Cu_3O_{7-\delta}$. *Physical Review B*, **54**, 1320–1333 (1996).

Spencer S and Jensen HJ. Absence of translational ordering in driven vortex lattices. *Physical Review B*, **55**, 8473–8481 (1997).

Täuber UC and Nelson DR. Interactions and pinning energies in the bose glass phase of vortices in superconductors. *Physical Review B*, **52**, 16106–16124 (1995).

Tinkham M. *Introduction to Superconductivity*. McGraw-Hill, 2nd edition (1996).

Tirado-Rives J and Jorgensen WL. Molecular-dynamics simulations of the unfolding of apomyoglobin in water. *Biochemistry*, **32**, 4175–4184 (1993).

van Otterlo A, Scalettar RT and Zimanyi GT. Phase diagram of disordered vortices from London Langevin simulations. *Physical Review Letters*, **81**, 1497–1500 (1998).

Verlet L. Computer 'experiments' on classical fluids. I. thermodynamical properties of Lennard-Jones molecules. *Phys. Rev.*, **159**, 98–103 (1967).

Watson GN. *Theory of Bessel functions*. Cambridge University Press, Cambridge, 2nd edition (1944).

Wilkin NK and Jensen HJ. Decoupling and melting in a layered superconductor. *Europhysics Letters*, **40**, 423–428 (1997a).

Wilkin NK and Jensen HJ. Disorder driven destruction of a phase transition in the vortex system of a superconductor. *Physical Review Letters*, **79**, 4254–4257 (1997b).

Yates K, Newman DJ and de Groot PAJ. Monte Carlo simulation of two-dimensional flux lattice melting. *Physica C*, **241**, 111–117 (1995).

Zhu BY, Xing DY, Dong J and Zhao BR. Dynamical phase transition of a driven vortex lattice with disordered pinning. *Physica C*, **311**, 140–150 (1999).